2019-11-16

The Variability of Winds and Fluxes Observed Near Submesoscale Fronts

Shao, Mingming; Ortiz-Suslow, David G.; Haus, Brian K.; Lund, Bjorn; Williams, Neil J.; Ozgokmen, Tamay M.; Laxague, Nathan J. M.; Horstmann, Jochen; Klymak, Jody M.

AGU

Shao, M., Ortiz-Suslow, D. G., Haus, B. K., Lund, B., Williams, N. J., Ozgokmen, T. M., et al. (2019). The variability of winds and fluxes observed near submesoscale fronts. Journal of Geophysical Research: Oceans, 124, 77567780.
http://hdl.handle.net/10945/66927

JGR Oceans

RESEARCH ARTICLE
10.1029/2019JC015236

The Variability of Winds and Fluxes Observed Near Submesoscale Fronts

Mingming Shao[1], David G. Ortiz-Suslow[2], Brian K. Haus[1], Björn Lund[1], Neil J. Williams[1], Tamay M. Özgökmen[1], Nathan J. M. Laxague[3], Jochen Horstmann[4], and Jody M. Klymak[5]

[1]Rosenstel School of Marine and Atmospheric Science, University of Miami, Miami, FL, USA, [2]Department of Meteorology, Naval Postgraduate School, Monterey, CA, USA, [3]Ocean and Climate Physics Division, Lamont-Doherty Earth Observatory, Columbia University, Palisades, NY, USA, [4]Helmholtz-Zentrum Geesthacht, Geesthacht, Germany, [5]School of Earth and Ocean Science, University of Victoria, Victoria, British Columbia, Canada

Key Points:
- Systematic ship-based observations of wind and fluxes across submesoscale fronts were conducted in varying wind directions
- Cross-frontal wind variance depended on the airflow relative to the in-water thermal gradient
- Submesoscale fronts were observed to locally enhance air-sea heat flux, compared to values from commonly used bulk algorithm

Correspondence to:
M. Shao,
mshao@rsmas.miami.edu

Citation:
Shao, M., Ortiz-Suslow, D. G., Haus, B. K., Lund, B., Williams, N. J., Ozgokmen, T. M., et al. (2019). The variability of winds and fluxes observed near submesoscale fronts. *Journal of Geophysical Research: Oceans*, *124*, 7756–7780. https://doi.org/10.1029/2019JC015236

Received 17 APR 2019
Accepted 1 OCT 2019
Accepted article online 26 OCT 2019
Published online 16 NOV 2019

Abstract Submesoscale oceanic fronts (SFs), which typically occur on a spatial scale of 0.1–10 km, may have a large influence on the atmospheric surface layer (ASL). However, due to their short temporal-spatial scales, evaluating their direct impact on this layer remains challenging and characterizing the nature of SF-ASL interaction has not been done in the field. To address this, a study of the air-sea response to SFs was conducted using observations collected during the Lagrangian Submesoscale Experiment, which took place in the northern Gulf of Mexico. This manuscript focuses on the meteorological measurements made from a pair of masts installed on the bow of the R/V *Walton Smith*. This work represents one of the first observation-based investigations into the potential influence that SFs have on the ASL. Contemporaneous measurements from an X-band marine radar, moving vessel profiler, and Lagrangian drifters were also used to analyze the SF dynamics. Systematic surface wind velocity changes over several cross-frontal transects were observed, a process previously associated with mesoscale fronts. A comparison between the eddy covariance and parameterized (COARE 3.5) air-sea fluxes revealed that the directly observed heat flux was 1.5 times larger than the bulk value in the vicinity of the SFs. This suggests that the hydrodynamic processes near the front enhance the local exchange of sensible and latent heat. Given the prevalence of SF over the global upper ocean, these findings suggest that these features may have a widely distributed and cumulative impact on air-sea interactions.

Plain Language Summary The atmosphere responds to the ocean over all scales—from microscopic to planetary scales. Previous studies showed that surface wind and even the entire atmospheric boundary layer could be affected by the relatively large-scale (10–1,000 km) temperature variations across the open ocean, for example, the Gulf Stream. However, the impacts of relatively small-scale (100 m to 10 km) and rapidly (hours to days) evolving fronts are largely unknown due to the difficulty in actually observing the physical processes. As part of an ongoing effort to better understand surface material dispersion across the northern Gulf of Mexico, we conducted ship-based measurements of air-sea fluxes across near small-scale fronts. The observations showed that the physical mechanism used to explain the interaction between the atmosphere and large-scale ocean temperature gradients readily downscales to these smaller fronts, which have a direct impact of wind directly above the ocean surface. These small-scale fronts were also observed to locally enhance the air-sea heat flux, and the conventional model used to predict this underestimates the observed value by as much as 50%. These small-scale frontal features are common across the global ocean, and our findings suggest that they could cumulatively impact the global energy budget.

1. Introduction

Frontal regions are common over the global ocean and usually accompanied by strong sea surface temperature (SST) gradients, where the coupling between the atmosphere and ocean becomes more complex. Most previous studies have focused on the coupling between the marine atmospheric boundary layer (MABL) and SST variability across mesoscale (10–1,000 km) fronts (Chelton & Xie, 2010), which exist mainly near the major western boundary currents, for example, Kuroshio current (Nonaka & Xie, 2003), Agulhas Current (O'Neill, 2012; O'Neill et al., 2012) and Gulf Stream (Chelton & Xie, 2010; Minobe et al., 2008; O'Neill, 2012;

O'Neill et al., 2017; Song et al., 2006; Plagge et al., 2016). The response of winds and surface fluxes to frontal zones was established from these previous satellite observational (Chelton et al., 2004) and modeling studies (Kilpatrick et al., 2014; Skyllingstad et al., 2007; Song et al., 2006). Wind speed and surface fluxes are usually enhanced over the warm water region with a thicker, well-mixed MABL and vice versa. Additionally, the surface atmospheric pressure is usually higher on the cold side of the front than the warm side.

Two main mechanisms for this acceleration or deceleration of surface wind across mesoscale SST fronts have been previously explored. The first mechanism is downward momentum transport. Wallace et al. (1989) observed that the maximum divergence of the surface winds occurred directly above the cold side of an oceanic frontal zone. They asserted that downward vertical mixing of momentum led to the surface wind variation. Recent numerical simulations support this view (Kilpatrick et al., 2014; Skyllingstad et al., 2007; Xu & Xu, 2015). Kilpatrick et al. (2014) showed that the direct response of the atmospheric surface layer (ASL) above the SST front was governed by nonrotating, internal boundary layer-like physics consistent with the vertical mixing mechanism. However, the vertical mixing mechanism may not account for the deceleration when the wind blows from the warm side to the cold side (Samelson et al., 2006). The second proposed mechanism is the pressure gradient adjustment. This view asserted that the surface pressure gradient effect across the front is the dominant term for the acceleration or deceleration of surface wind. The warming of the atmosphere over high-SST regions causes a reduction in pressure via hydrostatic balance, with a commensurate increase in pressure over the cooler water. This mechanism has been used to describe mesoscale surface wind-SST interactions (Lindzen & Nigam, 1987; Shi et al., 2017).

Limited field observations of air-sea interactions across fronts have been conducted in the open ocean (Friehe et al., 1991; Kwon et al., 1998; Romero et al., 2017; Vickers & Mahrt, 2006; Vihma et al., 1998) and shelf regions (Mahrt et al., 2004; Pezzi et al., 2016). According to these studies, these fronts were usually evaluated within a relatively larger spatial regime (10–100 km). These observations generally showed that the wind speed increases when the wind blew from the cold water across the front, with significant differences observed in the downwind structure of the air temperature (i.e., stability) and fluxes (Friehe et al., 1991; Mahrt et al., 2004). The momentum and sensible and latent heat fluxes respond strongly to SST changes, and Vickers and Mahrt (2006) estimated a threshold of 1 °C in SST amplitude over a horizontal scale of 8 km from their aircraft observation over a warm pool. Their aircraft data were mainly collected from 30–300 m above the surface, which missed the dynamics within the very near surface layer (0–10 m).

Due to the dynamic coupling of the atmosphere and ocean, the influence of transient, mesoscale structures at the ocean surface effectively creates an imprint of the upper ocean on the MABL (Frenger et al., 2013; Small et al., 2008). A similar process may also occur at the submesoscale regime (Gaube et al., 2019). Submesoscale fronts (SFs), one kind of oceanic submesoscale phenomena, can be detected by their surface expression. Typically, SFs are defined as a SST gradient spanning a horizontal distance of 0.1–10 km. They can spontaneously emerge during the evolution of mesoscale eddies (Capet et al., 2008). The dynamical character of SFs is often consistent with a combination of a surface density gradient and vertical momentum mixing by boundary layer turbulence (McWilliams, 2016). Submesoscale currents in the ocean have spatial scales of 0.1–10 km, time scales of hours to 1 day, and a dynamic scale with the Rossby number on the order of 1. The Rossby number is defined as

$$Ro = \frac{\Omega}{f}, \tag{1}$$

where the vertical vorticity is

$$\Omega = \left(\frac{\partial v}{\partial x} - \frac{\partial u}{\partial y} \right), \tag{2}$$

and (u, v) and (x, y) are horizontal spatial and velocity components respectively, and f is the local Coriolis parameter. Submesoscale currents are generated through a variety of ageostrophic instabilities associated with large-scale geostrophic currents (Klein et al., 2019; Sullivan & McWilliams, 2018; Taylor, 2018) and may substantially affect the energy cascade in the upper ocean. However, conventional current sensors (e.g., satellite altimetry) cannot generally capture the different structures of submesoscale currents (fronts, eddies, and filaments) due to their small spatial(<10 km) and temporal (hour to day) scale. Because of this, there has been a delayed appreciation for their abundance (Klein et al., 2019; McWilliams, 2016).

As a result of this general lack of attention on submesoscale currents, understanding of SF's role in ASL variability is also lacking. An idealized large eddy simulation by Wenegrat and Arthur (2018) showed that

the SF's impact could reach to the free atmospheric layer, but these results have not been validated by field observations. The assumed logarithmic vertical profile of wind speed indicates that there is a strong velocity gradient within the ASL, which produces the most energetic air-sea fluxes occurring in the MABL. The variability of the log layer across SF is unknown from previous aircraft measurements (Vickers & Mahrt, 2006) and satellite observation (Gaube et al., 2019).

Understanding the air-sea coupling mechanism near SFs is necessary as this coupling may significantly affect the upper ocean dynamics. For instance, observations of SF near the Kuroshio current indicated that a wind component along a SF catalyzed the release of energy from fronts to turbulence, and the rate of energy dissipation within the frontal boundary was enhanced by 1 or 2 orders of magnitude (D'Asaro et al., 2011). In addition, frontal regions are usually strong convergence zones, where chemical processes may be intensified owing to either high gradients of properties or vigorous air-sea interaction (Lohmann & Belkin, 2014).

Submesoscale processes have not been well parameterized and thus have not been included in current general ocean circulation models but could play a critical role in local air-sea interaction (Klein et al., 2019; McWilliams, 2016). Lambaerts et al. (2013) introduced submesocale filaments to a coupled ocean-atmosphere model and noticed that when submesoscales were more energetic, the vertical atmospheric velocities were much more intense. This indicates an important role played by submesoscale structures (fronts, eddies, and filaments) in the upper ocean and lower atmosphere. It has also been shown that atmosphere and ocean models need to be coupled at higher temporal resolution to allow resonant generation of near-inertial motion in the upper ocean (Byrne et al., 2016; MacKinnon et al., 2017) and to simulate the effect of air-sea interaction on western boundary current evolution (Ma et al., 2016; Renault et al., 2019). These modeling results also need to be validated with observations.

In summary, no systematic observation-based evaluation of the potential impacts of SF on the ASL has been accomplished using near-surface, air-sea measurements. The aim of this study is to use data from the the Lagrangian Submesoscale Experiment (LASER) campaign to analyze the atmospheric variability near SFs. The fronts were formed by the interaction between the Mississippi River plume and the continental shelf waters, which may also be affected by the Loop Current system in the Gulf of Mexico. The analysis presented here focused on measurements from the R/V *Walton Smith* where a combination of micrometeorological, upper ocean, and radar backscatter data were used to study SF-atmosphere interactions. This manuscript focuses on understanding the surface wind and air-sea flux variability across SFs. The relative performance between eddy covariance and bulk parameterizations of fluxes was also evaluated.

The field observation and data analysis methods are described in sections 2 and 3, respectively. Section 4 discusses the observation results, including cases when the wind blew from cold to warm water and conversely from warm to cold water. The relationship between SF and ASL and the enhancement of heat flux near SF are discussed in section 5. Results are summarized and future work is described in section 6.

2. Field Experiment

LASER was undertaken by the Consortium for Advanced Research on Transport of Hydrocarbon in the Environment (CARTHE, http://carthe.org/) as a large-scale effort to study the transport and dispersion of ocean surface contaminants. The main focus of the experiment was a massive Lagrangian drifter deployment ($\sim 1,000$ satellite tracked units) to illuminate the physics of surface transport and dispersion (D'Asaro et al., 2018; Poje et al., 2014). It took place in the northern part of the Gulf of Mexico from 12 January to 15 February 2016. SFs were mostly observed near the De Soto Canyon, where submesoscale processes played a key role in determining the horizontal mixing properties. The R/V *Walton Smith* (Figure 1a) was the main platform used during LASER for oceanographic and atmospheric sensor data collection. The focus of this study will be on the meteorological and oceanographic data collected, when the R/V *Walton Smith* was near the SFs.

2.1. R/V *Walton Smith* Data Collection and Processing

Eddy covariance (EC) measurements of momentum, heat, and water vapor fluxes were collected from the R/V *Walton Smith* during LASER. Because of its shallow-water twin hull design the R/V *Walton Smith* constitutes an excellent platform for air-sea interaction studies and similar vessels have been previously used for these near-surface studies (Katsaros et al., 1993). A flux tower was mounted on each of the prows, and each was outfitted with three flux levels (Figure 1). Ultrasonic anemometers (RM Young 81000) were mounted at 3.6 and 4.6 m above the mean surface, with a Campbell Scientific IRGASON (Integrated CO_2 and H_2O

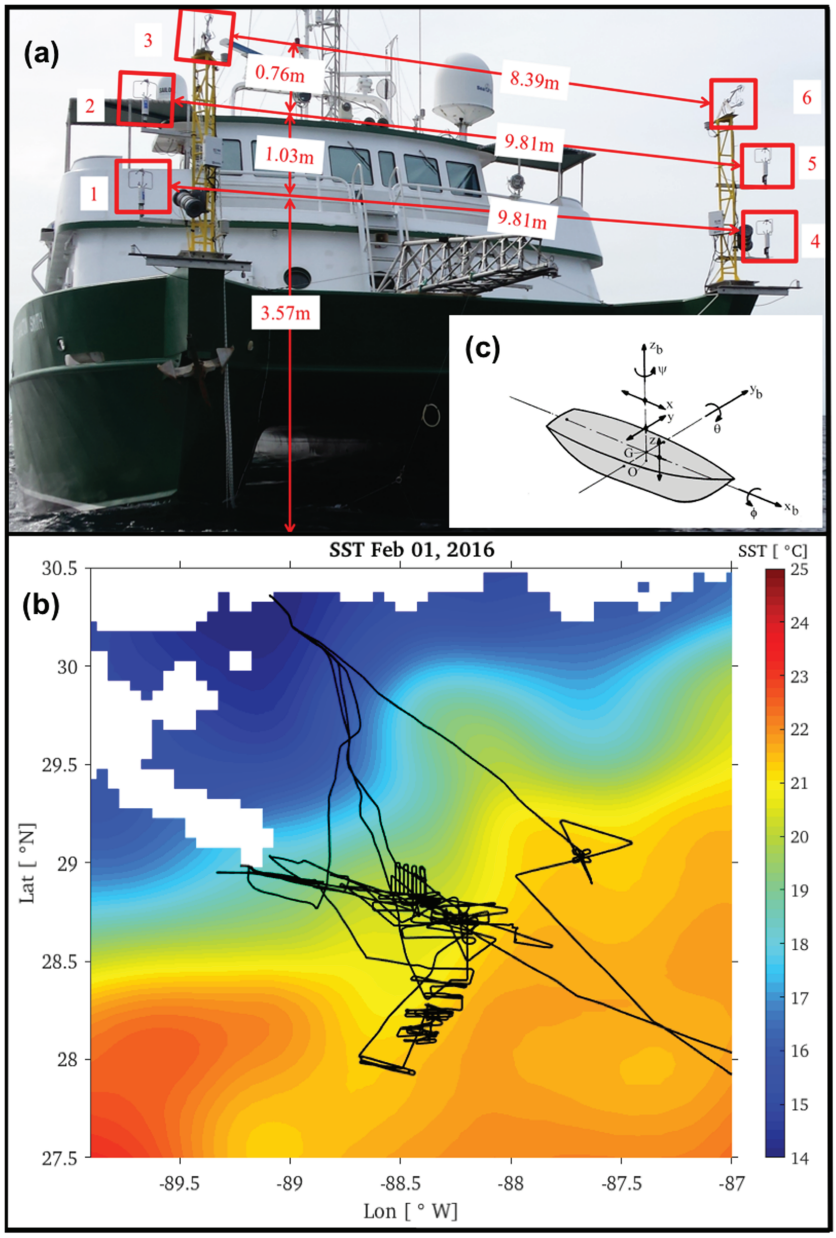

Figure 1. (a) R/V *Walton Smith* and twin flux towers employed during LASER. The anemometer number referenced in this study is given. The lowest anemometer was 3.57 m above the mean surface level. The vertical distances between z_3 and z_2, and between z_2 and z_1 were 0.76 and 1.03 m, respectively. The horizontal distances between y_3 and y_6, between y_2 and y_5, and between y_1 and y_4 were 8.39, 9.81, and 9.81 m, respectively. (b) Sea surface temperature (from OSTIA) acquired 1 February 2016. The black solid line represents the ship track during the entire LASER cruise. The OSTIA data can be accessed online (from http://podaac.jpl.nasa.gov/dataset/UKMO_L4HRfnd_GLOB_OSTIA). (c) The vessel coordinate system is centered at the motion pack, and it is defined so that X is parallel to the bow-stern axis (positive to the bow), Y is parallel to the port-starboard axis (positive to port), and Z follows from right-hand rule (positive upward). LASER = Lagrangian Submesoscale Experiment; OSTIA = Operational Sea Surface Temperature and Sea Ice Analysis.

Open-Path Gas Analyzer and 3-D Sonic Anemometer) mounted atop each tower (5.36 m above the mean surface). The RM Young anemometers only resolve the momentum and sensible heat flux, while the IRGASON resolves the momentum and total (sensible+latent) heat flux. Water surface elevation was simultaneously observed from a bow-mounted array of five ultrasonic distance meters (UDMs, Senix ToughSonic 30). This UDM array was mounted to the superstructure between the prows. The ship motion was measured using linear accelerometers (Columbia Research Model AS-307HPTX) and rotation rate gyros (SYSTRON Donner

QRS11-00050-630). Sea level pressure was measured by a Vaisala sensor (Vaisala PTB110) within the IRGASON data processing unit.

As a part of the standard measurement capability of the R/V *Walton Smith*, two downward looking Accoustic Doppler Current Profilers (ADCPs) were mounted on the bottom of the hulls about 1 m below the mean surface. One of the ADCPs was configured to sample near the surface (7–29 m) with a vertical resolution of 2 m. The uppermost velocity profile bins were used to represent the surface current used in the bulk algorithm: $U = |U_{\text{wind}} - U_{\text{current}}|$. One-minute ensemble averages were used, which produced profiles with a horizontal spacing ~220 m (at normal ship operation speed). The ADCP data were quality controlled and corrected for ship speed and heading using Common Ocean Data Access System developed by the University of Hawaii (https://currents.soest.hawaii.edu/docs/adcp_doc/codas_doc/codas_database.html).

Water temperature and salinity were sampled (6 Hz) using a flow-through system, SBE 45 MicroTSG (Sea-Bird MicroThermoSalinoGraphy), with an intake located 1 m below mean water level. In addition, a Rolls-Royce 300 moving vessel profiler (MVP) was deployed on the stern to measure salinity and temperature profiles while the ship was underway. The MVP is a weighted conductivity-temperature-depth (CTD) instrument that free falls at approximately 3 m/s and is returned to the surface by a winch. Casts to 160 m were recorded roughly every 200 m along the ship track with a vertical resolution of 1 m (D'Asaro et al., 2018).

A Helmholtz-Zentrum Geesthacht Marine X-band radar (MR) was mounted on a tower installed on top of the wheelhouse. The MR backscatter maps covered a 360° azimuthal range out to 3.1 km (maximum). These maps have a horizontal resolution of ~7.5 m. A recently developed algorithm (Lund et al., 2015, 2018) was used to derive surface current fields (500-m resolution) from the directly observed surface roughness. A comparison between MR and drifter (4,130 pairs, some drifter tracks are shown in Figures 3a, 7a, and 10a) retrieved currents resulted in a correlation of 0.94 with a root-mean-square error of 0.04 m/s in speed and 12.2° in direction, with a negligible bias (Lund et al., 2018).

2.2. Meteorological Data Quality Control

The data were synchronized by a Network Time Protocol Server and were routed into the main cabin and recorded by Campbell Scientific CR6 and CR3000 data-loggers at 20 Hz. Data segments with over 2% of the samples missing (due to synchronization errors or electronic noise) were rejected and not included in the flux processing. Segments were also rejected if the R/V *Walton Smith* heading over the segment deviated by $> 35°$. This was done to remove apparent cross-wind velocities due to the vessel's turning. In order to balance the demands of the EC technique, as well as resolve the spatial variability near the fronts, an averaging interval of 10 min was used for all the fluxes.

Another aspect of the data processing was outlier sample detection and removal. Spikes can arise from sea spray, rain, or spurious noise in the sonic anemometer. A Goring and Nikora (2002) type algorithm was used for this process. Identified spikes were removed from the time record, and the gap was filled using third-order polynomial interpolation. This despiking was carried out on the raw observations in 10-min segments. After this step, the 3-D wind velocity data were corrected for the platform's accelerations, rotations, and translations (Anctil et al., 1994). Motion-corrected data were included in the final data only if the wind direction relative to the heading was within ±90° of the R/V *Walton Smith* bow. Outside of this range, the wind was expected to be significantly affected by flow distortion around the vessel's superstructure and/or mast. Wind coming from ±20° of the R/V *Walton Smith* heading was considered as ideal conditions, where both masts could be considered unaffected by the vessel. As a result of the mean vessel heading relative to the wind direction (during the frontal transects analyzed for this study), the IRGASON from the starboard mast was the main source of the flux data.

The flux footprint quantifies the Lagrangian trajectory of the turbulent eddies that originate at a point upstream of the measurement location (Veron et al., 2008). Based on the method from Högström et al. (2008) and the observed atmospheric stability, from the IRGASONs, the upstream distance containing 80% of the measured flux was estimated to be on the order of 100 m. Thus, near the SFs, we expect the fluxes to be primarily locally generated.

2.3. Other Data Sources

Satellite SST data were used for the mesoscale frontal detection during the LASER cruise, which was obtained from the Operational Sea Surface Temperature and Sea Ice Analysis (OSTIA), a blended product

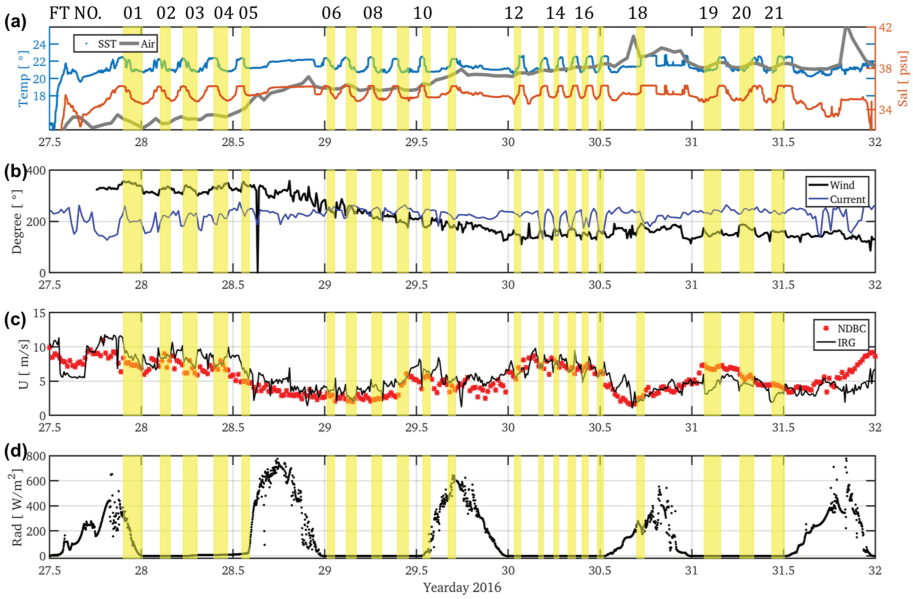

Figure 2. Overview of shipboard observations during the cross-frontal analysis days; the yellow shading represents individual frontal transects (some labels are not included for clarity). (a) MicroTSG temperature (blue), salinity (orange), and air temperature (gray); (b) 10-min wind (IRGASON) and Accoustic Doppler Current Profilers current (upper 10 m vertically averaged) directions; (c) 10-min averaged wind speed from IRGASON and 8-min averaged wind speed from NDBC (No.42887); (d) downwelling shortwave irradiance. NDBC = National Data Buoy Center.

using satellite data from infrared, visible, and radiometer sensors as well as in situ data from drifting and moored buoys (Pezzi et al., 2016). The data sets are available daily on a 0.1° grid. Here the SST map of 1 February 2016 was chosen to represent the mesoscale SST features (Figure 1b) during the front-crossing days.

The R/V *Walton Smith* meteorological observations were compared to a nearby National Data Buoy Center (NDBC) platform (42887) for the entire LASER experiment (Figure 2c). NDBC 42887 is an oil platform located 10–20 km away from the study region (28.191°N, 88.496°W; see Figures 3 and 7).

3. Analysis Methods

The two most widely used methods for quantifying the air-sea fluxes are EC and bulk parameterization. EC is the most widely used technique for directly measuring the fluxes, but it requires more robust sensors and more in-depth data processing (as described above); while the bulk parameterizations (of which there are several in the literature) are statistical representations of observed variability from field studies (usually using the EC method). Ultimately, both methods seek to provide an estimate of the turbulent quantities necessary to compute the air-sea fluxes. Here, the bulk algorithm COARE 3.5 (Edson et al., 2013) was used, which is an update of early COARE algorithms (Fairall et al., 1996, 2003). The following section will briefly summarize the theoretical basis for both methods.

3.1. The EC Technique

Momentum flux (τ) is composed of the covariance between the vertical fluctuation velocity and along cross-wind fluctuation components, respectively. It is defined as

$$\vec{\tau} = -\rho(\overline{u'w'}\hat{\imath} + \overline{v'w'}\hat{\jmath}), \tag{3}$$

where ρ is the air density, and w', u', and v' are the turbulent fluctuations of vertical and horizontal along-wind and cross-wind velocities. The overline represents a suitable averaging interval (here 10 min was chosen). The window applied for this study corresponds to a horizontal displacement of ~2 km, assuming a mean ship speed 3–4 m/s. The appropriate time scale for averaging depends on the regime of interest. For example, Ortiz-Suslow et al. (2015) used a 5-min window in order to analyze the spatially heterogeneous nearshore region, while Geernaert and Richter (1986) chose a 57-min window to achieve the greatest statistical reliability of the low frequency turbulence spectrum.

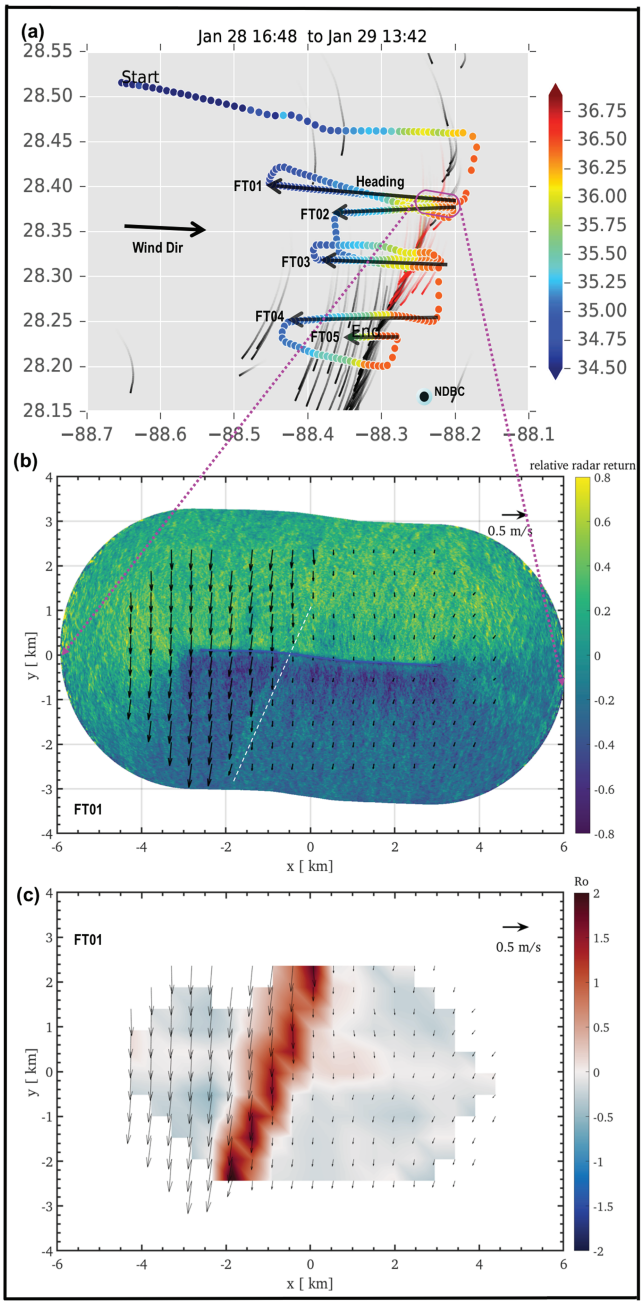

Figure 3. SF position and one radar image of SF in CW group. (a) Ship track colored by the surface salinity during the CW group. The arrows represent the ship's heading at SF boundary, and the corresponding FT number is given. The dark lines represent the last 24 hr of drifter trajectories. The location of NDBC 42887 is also marked by the black dot. (b) Expanded view of the radar-derived backscatter intensity in the magenta eclipse region in (a). The front location was highlighted by a adjacent white dashed line. The corresponding surface current map was derived from the 3-D wavenumber frequency radar image spectrum (Lund et al., 2018). The blue line denotes the ship track during this time. (c) Expanded view of surface Rossby number resulting from (b). The vectors are the same as the vectors in (b). SF = submesoscale oceanic fronts; NDBC = National Data Buoy Center.

Sensible heat flux (SHF) was calculated as

$$SHF = -\rho C_p \overline{w'\theta'}, \tag{4}$$

where C_p is the air heat capacity and θ' is the potential temperature fluctuating component. Latent heat flux (LHF) was calculated as

$$LHF = -\rho L_e \overline{w'q'}, \tag{5}$$

where q is the specific humidity and L_e is the latent heat of vaporization.

3.2. Bulk Algorithm

The bulk formula for the momentum flux is

$$\tau_c = \rho C_d (U - U_c)^2, \tag{6}$$

where C_d is the drag coefficient, U is the wind speed at certain height z, and U_c is representative of the surface current component parallel to the mean wind vector. The bulk algorithm for the SHF is

$$SHF_c = \rho C_p C_h (U - U_c)(\theta_s - \theta), \tag{7}$$

where C_h is sensible heat exchange coefficients and θ_s is the surface radiative temperature. The formula for LHF is

$$LHF_c = \rho L_e C_q (U - U_c)(q_s - q), \tag{8}$$

where q_s is the specific humidity at saturation and C_q is latent heat exchange coefficient.

The COARE 3.5 bulk algorithm (Edson et al., 2013) was improved from COARE 3.0 (Fairall et al., 1996, 2003), with options for parameterizing the surface roughness (z_0) using wave age and/or significant wave height (in addition to the default/conventional wind speed dependence). All the exchange coefficients (C_d, C_h, C_q) are height, stability, and roughness length dependent, which can be standardized to neutral conditions at 10 m using Monin-Obukhov similarity theory,

$$C_d = \left[\frac{\kappa}{\ln(z/z_{om}) - \psi_m}\right]^2, \tag{9}$$

$$C_h = \left[\frac{\kappa}{\ln(z/z_{om}) - \psi_m}\right]\left[\frac{\kappa}{\ln(z/z_{oh}) - \psi_h}\right], \tag{10}$$

$$C_q = \left[\frac{\kappa}{\ln(z/z_{om}) - \psi_m}\right]\left[\frac{\kappa}{\ln(z/z_{oq}) - \psi_q}\right], \tag{11}$$

where ψ_m, ψ_h, ψ_q are the stability functions, which are all functions of ζ, and z_{om}, z_{oh}, z_{oq} are the roughness lengths for momentum, temperature, and moisture. κ is the Von Kárman constant, and here $\kappa = 0.4$ (Tennekes et al., 1972). Stability parameter $\zeta = z/L$ (Monin & Obukhov, 1954). Here L is given by

$$L = \frac{u_*^3 \overline{\theta_v}}{g\kappa \overline{w'\theta_v'}}, \tag{12}$$

where θ_v is the virtual temperature in air, and θ_v' is the fluctuating component of virtual temperature. $u_* = \sqrt{\frac{\tau}{\rho}}$ is the friction velocity. The stability function for momentum is

$$\psi_m(\zeta) = \begin{array}{l} 2ln\left(\frac{1+x}{2}\right) + ln\left(\frac{1+x^2}{2}\right) - 2tan^{-1}(x) + \frac{\pi}{2}; \zeta < 0, \\ -a_2\zeta; \zeta > 0, \end{array} \tag{13}$$

where $x = (1 - a_1\zeta)$, $a_1 = 16$, and $a_2 = 5$. For ψ_h and ψ_q, the same expression is used:

$$\psi_h(\zeta) = \psi_q(\zeta) = \begin{array}{l} 2ln\left(\frac{1+x}{2}\right); \zeta < 0, \\ \psi_m(\zeta); \zeta > 0, \end{array} \tag{14}$$

Table 1
Table Summarizing the Conditions and State of Each Frontal Transect Collected as Part of This Study

Group	FT	Date	Start–end	Hours	U (m/s)	θ_{wind} (°)	U_c (m/s)	θ_{cur} (°)	H_s (m)
CW01	01	28 Jan	21:37–23:59	2.5	8.3	347.9	0.5	207	2.1
CW02	02	29 Jan	02:27–03:47	1.3	8.5	327.8	0.5	216.6	1.8
CW01	03	29 Jan	05:27–07:17	1.8	7.7	327.6	0.6	221.3	1.8
CW02	04	29 Jan	09:27–11:17	1.8	7.6	335.2	0.7	209.5	1.7
CW01	05	29 Jan	13:07–14:07	1.0	6.5	342.5	0.6	217.4	1.5
	06	30 Jan	00:17–01:17	1.0	3.4	238.9	0.3	247.0	1.0
	07	30 Jan	02:47–04:07	1.3	2.4	249.7	0.5	261.0	0.8
	08	30 Jan	06:27–07:27	1.3	4.3	212.1	0.4	252.0	0.7
	09	30 Jan	09:27–10:57	1.5	5.5	196.2	0.3	263.9	0.6
	10	30 Jan	12:47–13:47	1.0	6.6	180.3	0.3	237.9	0.7
	11	30 Jan	16:07–17:07	1.0	4.9	178.5	0.3	226.0	0.8
	12	31 Jan	00:47–01:37	0.83	5.9	147.8	0.3	222.8	0.9
WC01	13	31 Jan	03:57–04:37	0.67	7.0	157.3	0.3	149.0	1.6
	14	31 Jan	05:57–06:37	0.67	7.4	163.2	0.4	144.9	1.6
WC01	15	31 Jan	07:47–08:47	1.0	6.6	167.5	0.3	183.0	1.7
WC01	16	31 Jan	09:37–10:27	0.83	6.2	151.3	0.3	183.3	1.6
WC01	17	31 Jan	11:37–12:27	0.83	6.1	160.1	0.4	159.0	1.8
	18	31 Jan	16:47–17:47	1.0	2.1	182.2	0.4	223.6	1.2
WC02	19	1 Feb	01:37–03:47	2.17	3.9	151.9	0.3	237.0	1.6
	20	1 Feb	06:17–08:07	1.83	4.5	179.5	0.3	243.4	1.5
WC02	21	1 Feb	10:27–12:07	1.67	3.1	159.5	0.4	233.9	1.5

Note. FT denoted the transect across the front. Rows without a group identified were not included in the final analysis. The columns are labeled as follows: Group identified, Front transect No., Date (of 2016) and start-stop time stamps (UTC), "U" represents the mean wind speed (z = 5.36 m), θ_{wind} is the corresponding wind direction, U_c is the mean current speed (from ADCP), θ_{cur} is the corresponding direction, and H_s is the significant wave height.

All of the ψ_x presented here follow from Businger et al. (1971).

COARE 3.5 is an empirical model based on many observational data sets collected from across the global, open ocean—excluding ship-based measurements in the 3.5 update. Buried within the experimental data variance used to develop COARE are many near-surface atmospheric and oceanic processes that may, individually, represent a break-down in the assumptions to develop the bulk formulae, for example, SFs. However, COARE does not isolate the contribution or impact of SF to the fluxes, and therefore doing a comparison between EC and bulk techniques may highlight the separate impact SF have on the air-sea exchange. This method of testing against bulk parameterizations has been used to assess the impact of nonresolved processes in previous works, for example, over complex nearshore regions (Ortiz-Suslow et al., 2015, 2018).

3.3. Identifying Fronts

SFs can be defined by gradients or discontinuities in temperature, salinity, density, velocity, and/or surface roughness. In this study, SFs were identified by SST gradients (> 1.5 °C over 5 km) and sea surface salinity (SSS) gradients (>1.5 psu over 5 km). MR backscatter intensity images were also used to corroborate the SST/SSS-identified SF and, in general, it was found that there was fairly good correspondence (Figures 3b, 7b, and 10b). In order to describe the ship observations across several SFs, a reference position along each front was set as the $x = 0$, and all cross-frontal distances were referenced to this "origin" (Figures 3b, 7b, and 10b). In two cases, FT02 (FT denoted the transect across the front) and FT03, the 0 location was determined by SST/SSS alone, due to a gap in the radar backscatter image record. Combining the in situ hydrography and the near-field remote sensing provided a very precise (within 100 m) means of locating each SF, as well as its orientation relative to the ship and its primary length scale (Figures 3c, 7c, and 10c). Details regarding all identified fronts included in this analysis are given in Table 1.

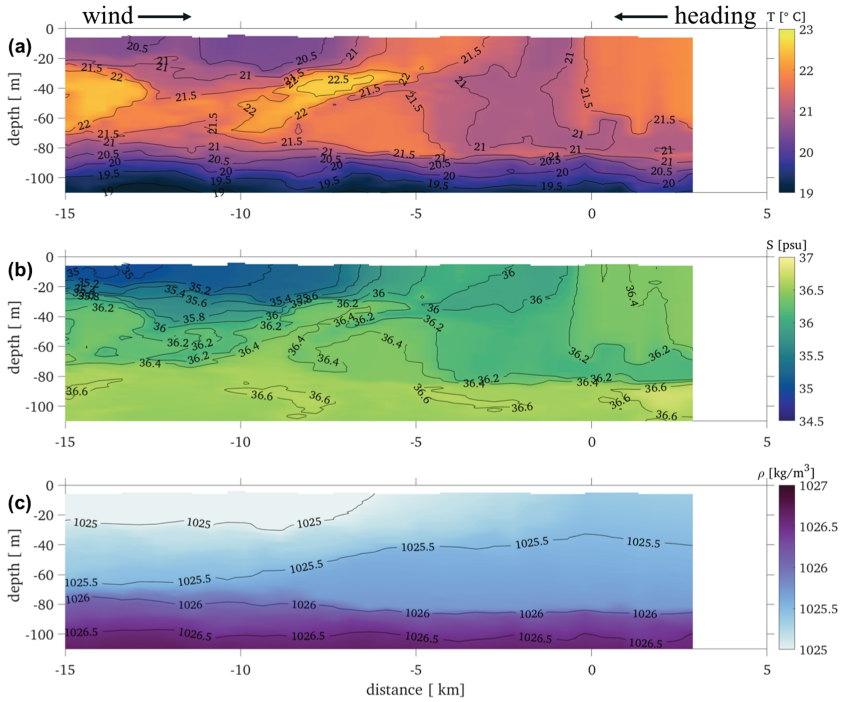

Figure 4. Vertical profiles along FT01. Wind is coming from left to right, and the R/V *Walton Smith* is translating from right to left. Front position denoted by "0." Temperature (a), salinity (b), and density (c) profiles derived from the moving vessel profiler are contoured.

3.4. Cross-Front Momentum Budget

The mechanism responsible for the wind speed variation near SFs has not been explored from observational data. To understand the relative importance of the different terms in the momentum budget, we calculated them from the multiple sensors distributed horizontally and vertically on the twin flux towers, which provided a unique opportunity to estimate most of the terms explicitly. The method is similar to Högström et al. (2013), in which the authors estimated the production and dissipation terms from tower based measurements.

The positive "X" direction was defined in the mean downstream wind direction, "Z" was defined as vertically upward and the other components follow from the right-hand rule. Before analysis, the wind direction over the transect length (typically 0.5–1.5 hr) was inspected and confirmed to be within a margin of ±20° from the initial value. Frontal orientation was assumed stationary over the transect. The cross-front momentum equation consists of the following terms:

$$\frac{\partial u}{\partial t} = \underbrace{-u\frac{\partial u}{\partial x} - v\frac{\partial u}{\partial y} - w\frac{\partial u}{\partial z}}_{\text{ADV}} + \underbrace{fv}_{\text{Cor}} \underbrace{-\frac{1}{\rho}\frac{\partial p}{\partial x}}_{\text{PG}} + \underbrace{\left(\frac{\partial \overline{u'w'}}{\partial z} + \frac{\partial \overline{u'u'}}{\partial x} + \frac{\partial \overline{u'v'}}{\partial y}\right)}_{\text{TSD}}. \tag{15}$$

The right-hand-side includes advection (ADV), Coriolis force (Cor), pressure gradient (PG), and turbulent stress divergence (TSD). In this context, Cor can be neglected because it is 2 orders of magnitude lower than the other terms. Due to the platform translation, the $\frac{\partial u}{\partial t}$ was not directly resolved.

Although the data had been selected based on common quality control criteria (section 2.2), some of the data may still be affected by flow distortion from the ship bow that is hard to quantify. Two kinds of flow distortions were mainly considered in the estimations: (1) The bottom anemometers ("1" and "4" in Figure 1) were consistently impacted by the flow distortion. After checking the data, these two levels from both masts were not included in the analyzed data; (2) When the wind was coming from the starboard side of the ship, the starboard tower was considered to be less affected by the flow distortion than port tower, and vice versa for the port side. The wind was consistently blowing from the starboard side for most of the frontal crossings, for this reason, the starboard tower top two levels were mainly used for the estimation.

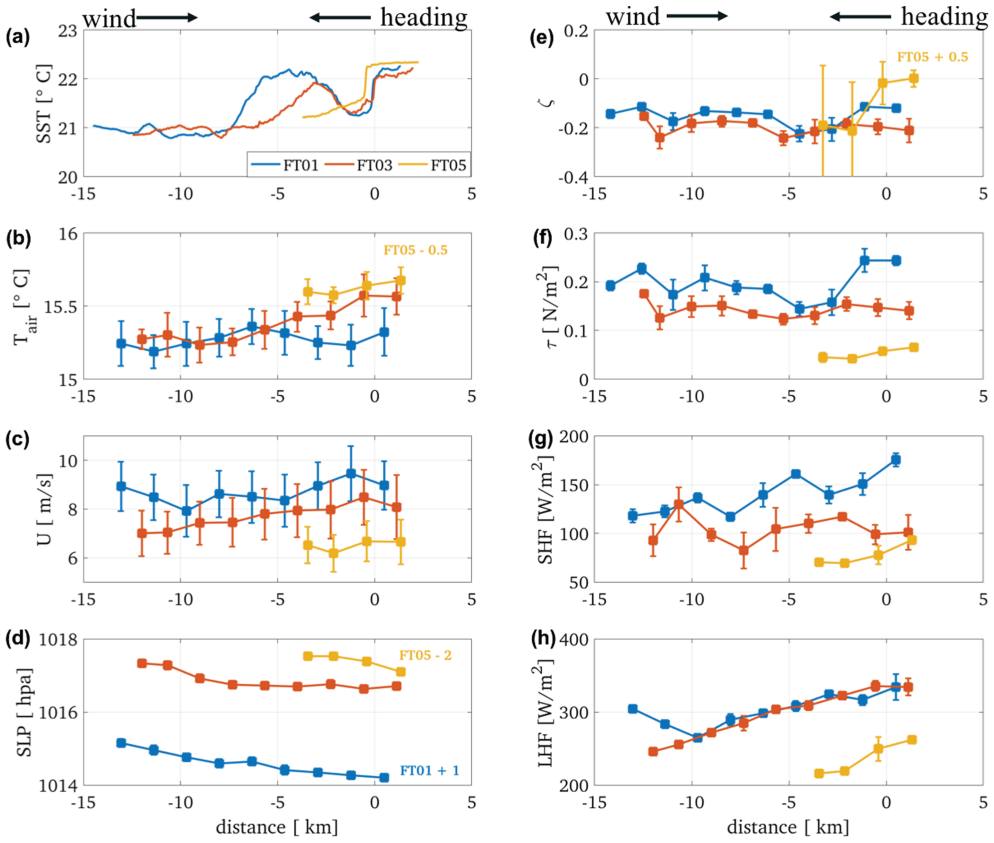

Figure 5. Observations from the starboard tower during the CW1 cross-frontal transects. (a) Sea surface temperature from flow-through MicroTSG, (b) air temperature, (c) 10-min averaged wind speed ($z = 5.3$ m), (d) pressure ($z = 5.3$ m), (e) Monin-Obukhov stability parameter (ζ), (f) momentum flux, (g) sensible heat flux, and (h) sensible heat flux derived using eddy covariance. The error bars indicate one standard deviation over each 10-min segment.

Considering the flow distortion above, the ADV term was estimated using a backward difference discretization:

$$u\frac{\partial u}{\partial x} = u_3\frac{u_3^i - u_3^{i-1}}{x_3^i - x_3^{i-1}}, \tag{16}$$

$$v\frac{\partial u}{\partial y} = v_3\frac{u_3 - u_6}{y_3 - y_6}, \tag{17}$$

$$w\frac{\partial u}{\partial z} = w_3\frac{u_3 - u_2}{z_3 - z_2}, \tag{18}$$

the velocity components and locations are given in Figure 1a, and i represents the ith velocity segment along a certain track. The PG term was estimated similarly as

$$\frac{\partial P}{\partial x} = \frac{P^i - P^{i-1}}{x^i - x^{i-1}}, \tag{19}$$

where P^i is the mean value of sea level pressure at i segment, and x^i is the position in the along wind direction. Finally, the TSD terms were estimated as

$$\frac{\partial \overline{u'v'}}{\partial y} = \frac{\overline{u'_3v'_3} - \overline{u'_6v'_6}}{y_3 - y_6}, \tag{20}$$

$$\frac{\partial \overline{u'w'}}{\partial z} = \frac{\overline{u'_3w'_3} - \overline{u'_2w'_2}}{z_3 - z_2}, \tag{21}$$

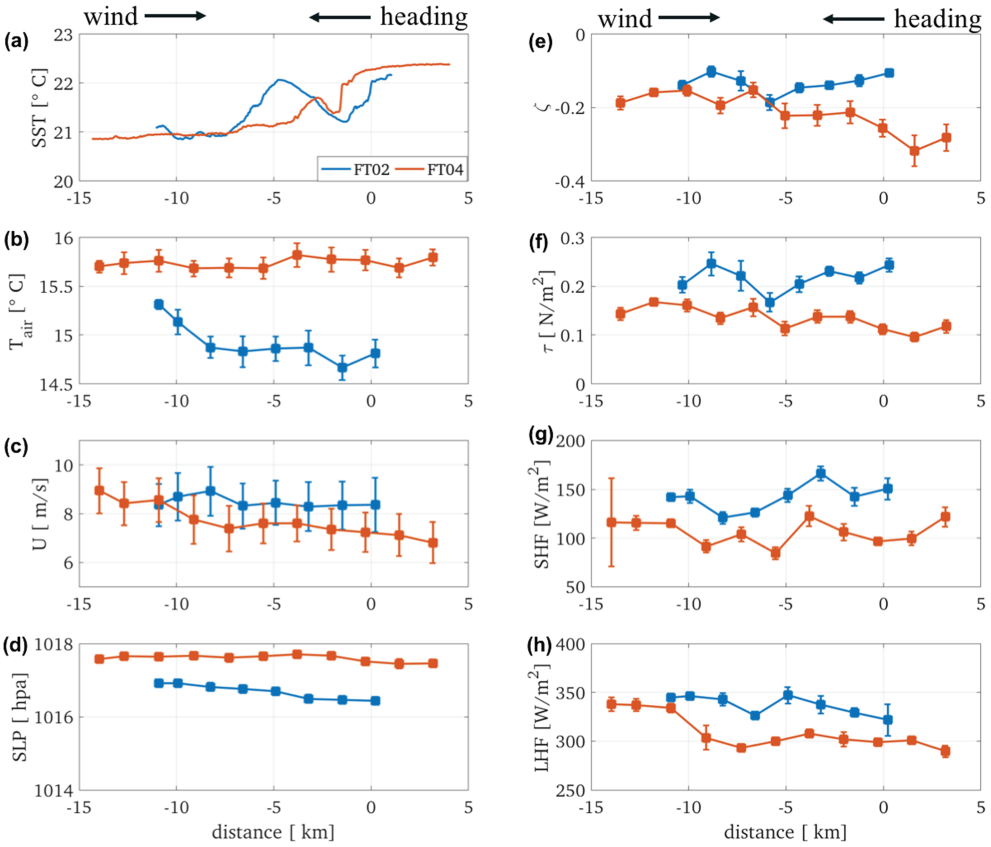

Figure 6. Observations from the starboard tower during the CW (anomalous) cross-frontal transects. (a) Sea surface temperature from flow-through MicroTSG, (b) air temperature, (c) 10-min averaged wind speed ($z = 5.3$ m), (d) sea level pressure ($z = 5.3$ m), (e) Monin-Obukhov stability parameter (ζ), (f) momentum flux, (g) sensible heat flux, and (h) latent heat flux derived using eddy covariance. The error bars indicate one standard deviation over each 10-min segment.

$$\frac{\partial \overline{u'u'}}{\partial x} = \frac{\overline{u'_3 u'^i_3} - \overline{u'_3 u'^{i-1}_3}}{x^i_3 - x^{i-1}_3}. \tag{22}$$

TSD terms were determined from the three-dimensional wind velocity using a 10-min average for the covariances. In this convention and because only cases where the ship was heading into the wind were studied, $u\frac{\partial u}{\partial x} < 0$ indicates flow deceleration.

4. Results

From 28 January 28 to 1 February 2016, the R/V *Walton Smith* transected 21 SFs where the ship heading was generally perpendicular to the frontal boundary (Figures 3a, 7a, and 10a). Over these 4 days, the air-sea temperature difference increased from −5 °C to ∼ 0 °C (Figure 2a), causing a shift in stability from unstable to near-neutral conditions. A few stable periods were observed as well. For the present analysis, 11 cases were chosen to focus on, where the wind was blowing generally perpendicular to the front (see shaded regions in Figure 2a). FT06–FT11 were not considered for this study because the wind was along front, which would invalidate the cross-frontal analysis and momentum budget. All of the frontal crossings occurred at night (except FT01, at twilight), where the ASL is expected to be stable (in terms of ζ; see shaded regions in Figure 2d). Also, during these 4 days, the wind direction shifted ∼ 180° (Figure 2b), providing an opportunity to compare the results of wind blowing from the cold side of the front to the warm side (CW) and conversely from warm to cold sides (WC). These two scenarios present a chance to compare the observed impact of SF to previous observations at the mesoscale, which showed the wind adjusts from a strong vertical gradient

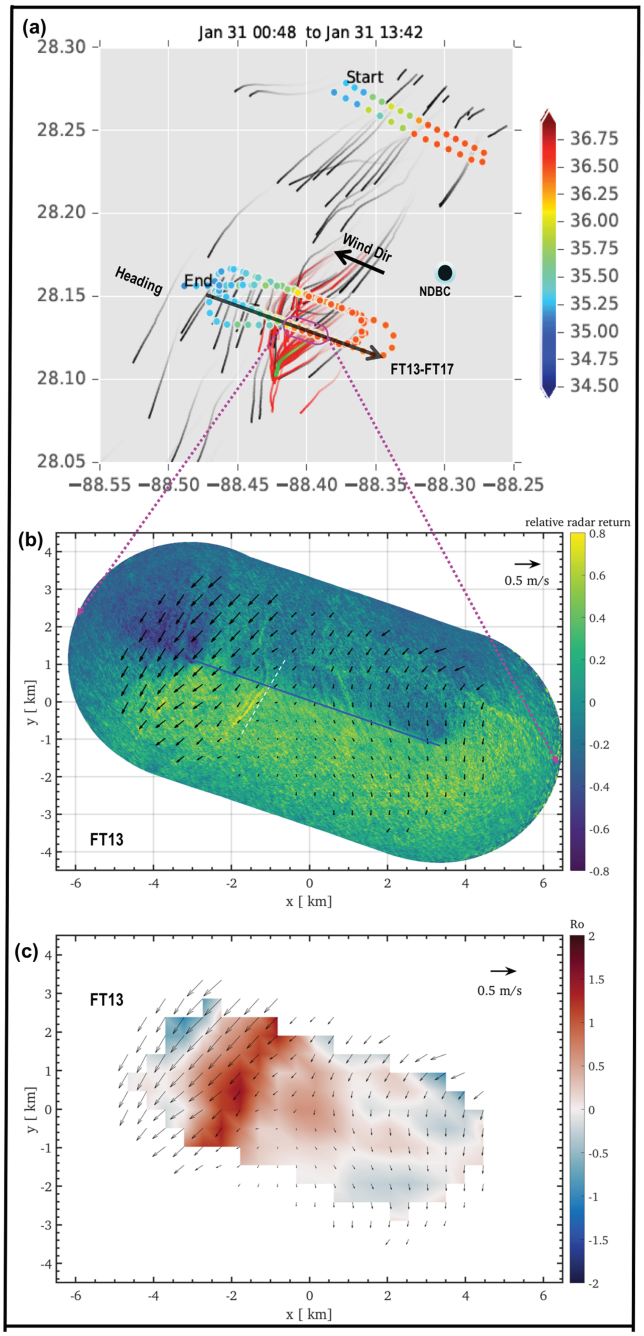

Figure 7. Similar to Figure 3, but for the WC1 group.

to a more homogeneous profile in CW transitions with decreasing sea level pressure (and vice versa). In this analysis, we will use CW (WC) conditions as a means of generally differentiating the expected SF-ASL interactions.

For all cases studied, the surface *Ro* was calculated from the MR-derived surface current map. Near the frontal boundary, all *Ro* were ~1, indicating that the saline submesoscale features had local vorticity slightly larger than, or comparable to, the local Coriolis parameter. The spatial characteristics of these SFs are also consistent with previous SF features (Taylor, 2018; Thomas et al., 2008), with horizontal scales 0.1 to 10 km across SST gradient.

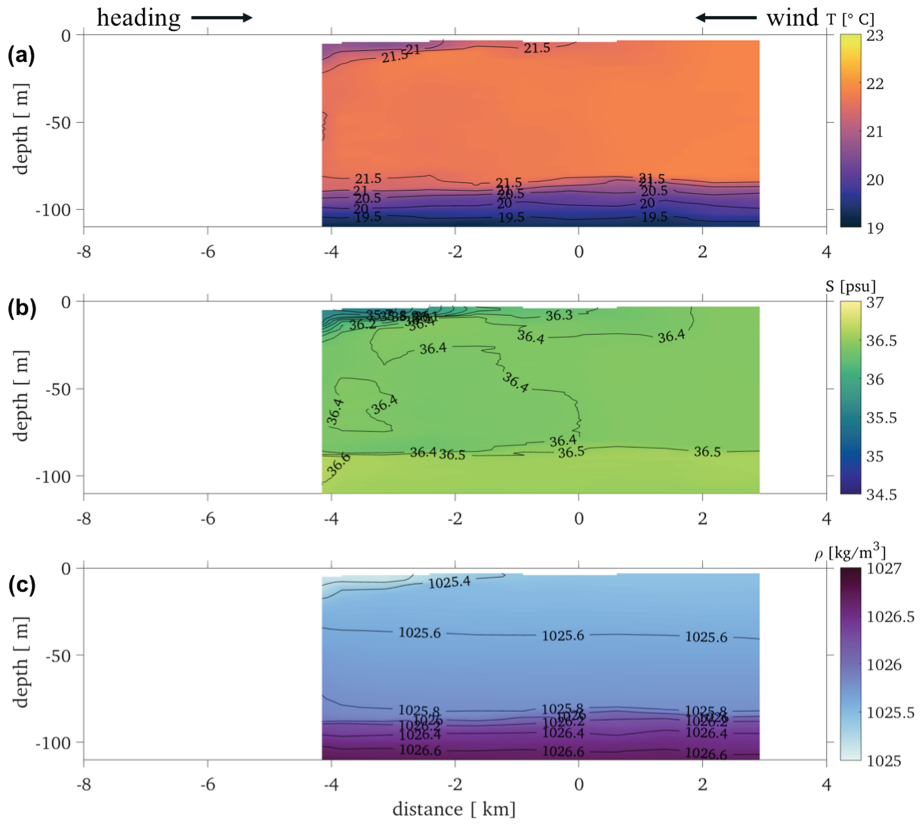

Figure 8. Vertical profiles along FT13. Wind is coming from right to left, and the R/V *Walton Smith* is translating from left to right. Front position denoted by "0." Temperature (a), salinity (b), and density (c) profiles derived from the moving vessel profiler are contoured.

4.1. The Observed ASL Response to SFs

4.1.1. Cold to Warm Transition in Moderate Winds

FT01 to FT05 were categorized as the CW group (Figure 3a and Table 1). FT01, FT03, and FT05 were grouped together (CW1, Figure 5) as they were associated with increasing wind speed from cold-to-warm; in sections 4.1.2, FT02 and FT04 (CW2, Figure 6) will be described separately because they exhibited a decreasing wind speed from cold-to-warm.

An example of the vertical MVP profiles of water temperature and salinity along FT01 transect are given in Figure 4. The CW1 group exhibited a consistent vertical structure of temperature and salinity, except for FT05, for which the cross-frontal span was shorter. The buoyant (colder and fresher) water occupied the upper 30 m on the upwind side and the subduction of cold water (−3.3 to 0 km, Figure 4a) indicated the convergence and downwelling of the front. The analogous subduction phenomena had been observed in other frontal regions in this data set.

SST was not monotonically decreasing along all the transects but exhibited a 6-km-wide mixing region with a 1.5-km-wide low-temperature patch on the warm side (Figure 5a). This cold patch was associated with the density-compensated subduction to 80 m (Figure 4a). The air-sea temperature difference for the entire FT01 track was generally −5 °C, corresponding to $\zeta \sim -0.2$, which, for this analysis, was considered to be the cutoff between near-neutral and unstable conditions. While it was difficult to discern a clear increasing air temperature trend from cold-to-warm (Figure 5b), the ASL was unstable across the entire transect (Figure 5e). Additionally, the sea level pressure decreased ~0.5 hPa from the cold side to the warm side for all three cases (Figure 5d).

There was a general trend of increasing wind speed in CW1. The wind speeds increased around 12–20% within 10 km along FT01 (8 → 9 m/s, Figure 5c) and FT03 transects (7 → 8.5 m/s, Figure 5c). Wind speed also increased 7% (+0.5 m/s) along FT05, in spite of its relatively short transect (~5 km). Correspondingly, along FT01, the momentum flux increased 67% (0.15 → 0.25 N/m^2) across the distance that the SST increased by

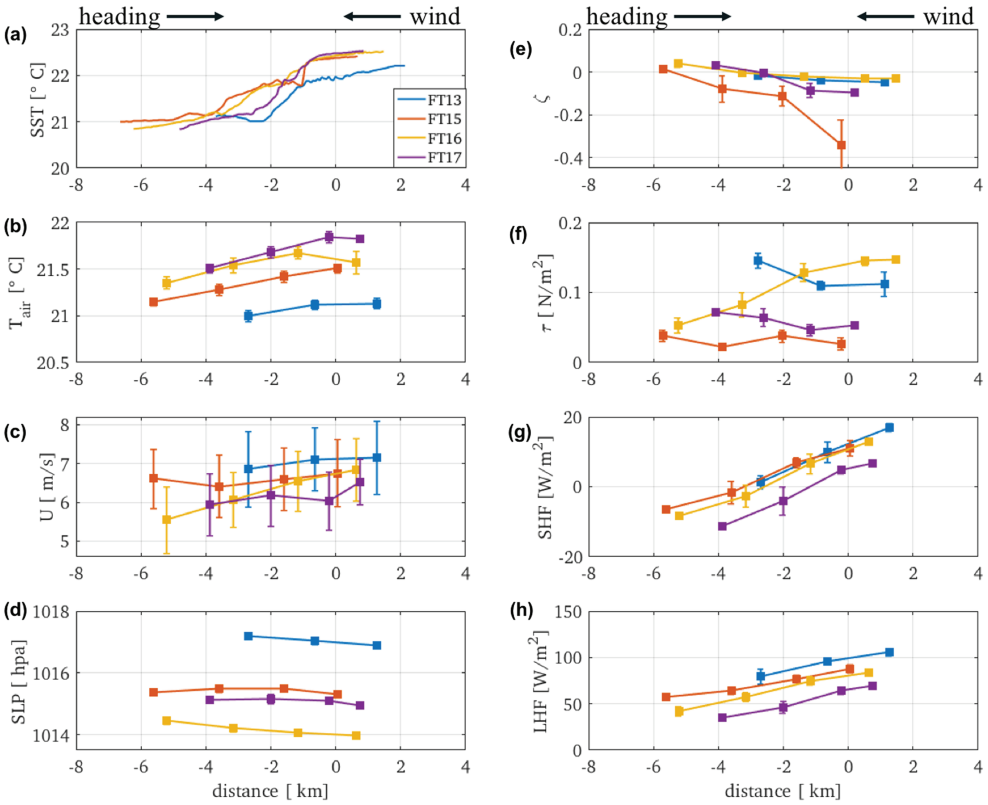

Figure 9. Observations from the starboard tower during the WC1 cross-frontal transects. (a) Sea surface temperature from flow-through MicroTSG, (b) air temperature, (c) 10-min averaged wind speed ($z = 5.3$ m), (d) sea level pressure ($z = 5.3$ m), (e) Monin-Obukhov stability parameter (ζ), (f) momentum flux, (g) sensible heat flux, and (h) latent heat flux derived using eddy covariance. The error bars indicate one standard deviation over each 10-min segment.

1.5 °C (from −2.5 to 0 km; Figure 5f). Momentum flux was effectively constant for FT03 (0.15 N/m^2), but did exhibit a 50% increase (0.5 → 0.75 N/m^2) across the entire FT05.

For CW1, the variability of SHF tended to coincide with the local changes in SST across the front (Figure 5g), increasing 50 W/m^2, for FT01 and FT03, over the −7.5- to −2.5-km span across which SST increased ~1.5 °C, but losing 40% (20 W/m^2) of this increase over the low SST region (−2.5 to 0 km). For the LHF, an increase of 100, 130, and 70 W/m^2 for FT01, FT03, and FT05, respectively, was observed (Figure 5h). The net relative change (average value in the warm side compared to the cold side) of LHF (10%) was less than SHF (30%).

4.1.2. Anomalous Cold to Warm Transitions

FT02 and FT04 showed distinct wind and flux variability from CW1 (Figure 6). In general, SST increased 1.5 °C from CW, with a low SST region between −5 and 0 km along FT02 (Figure 6a). During FT02 transect, the air temperature decreased by 0.8 °C from −10 to 0 km (Figure 6b), while ζ increased from −0.2 to −0.1 (Figure 6e) and sea level pressure decreased by 0.5 hPa (Figure 6d). For FT04, although SST increased by 1.5 °C (Figure 6a), air temperature was almost constant (~ 15.7 °C, Figure 6b), ζ decreased from −0.2 to −0.3 (Figure 6e), and sea level pressure was constant (Figure 6d).

For FT02, the wind speed decreased from 9 to 8.5 m/s (−8.5 to −5 km) and then leveled off to ~8.2 m/s (Figure 6c), which corresponded to a 28% drop in momentum flux (Figure 6f, −8.5 to −5.5 km). Independent of the wind speed and over the range −5 to −2 km, momentum flux regained this initial drop and increased from 0.18 → 0.25 N/m^2 (Figure 6f). Though the overall transect was in CW condition, the wind over this localized decreased SST (−5 to −2 km) was in WC condition. Thus, the increased momentum flux (Figure 6f, −5 to −2 km) coincided with the localized decrease in SST over this portion of the transect (Figure 6a, −5 to −2 km). Along the FT04 transect, the wind speed dropped by 22% (9 → 7 m/s) within 15 km, while momentum flux decreased by 37.5% (0.16 → 0.10 N/m^2).

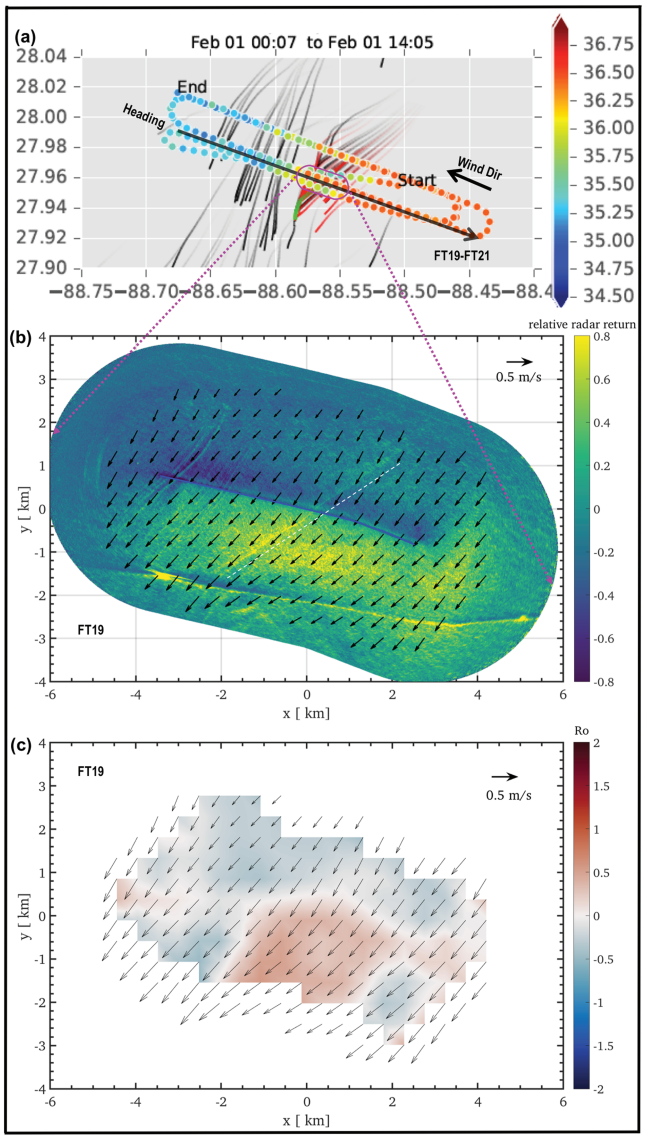

Figure 10. Similar to Figure 7, but for the WC2 group.

SHF increased 30 W/m^2 along FT02 (from −8.5 to −3 km, Figure 6g) over the increasing SST range. However, SHF was generally constant (110 W/m^2) along FT04, with some variability observed near a localized SST warm pool (from −5.5 to −4 km). In contrast to the variation of SHF, LHF decreased 40 and ~50 W/m^2 for FT02 and FT04, respectively. The variation of LHF did not show an obvious trend with local SST variation.

4.1.3. Warm to Cold Transition in Moderate Winds

FT13 through FT17 were categorized as the WC1 group. They occurred during moderate winds ($5 < U <$ 10 m/s). This subgroup is unique because the R/V *Walton Smith* transected the same front five times, over an 8-hr period, which helped to build statistical confidence in quasi-stationary ocean surface conditions. The SF did not show subduction of surface waters (Figure 8) and drifter tracks were not concentrated along the frontal boundary (Figure 7a), indicating that this particular front was not a convergence zone. Therefore, SST in WC1 was generally found to monotonically decrease along each transect (Figure 9a). For WC1, a lens of colder, fresher water occupied the upper 20 m of the water column starting approximately 1 km downwind of the front (Figure 8).

Within ~4 km downwind of the frontal boundary, SST was observed to decrease by 1.5 °C across all four transects (Figure 9a). Simultaneously, air temperature decreased between 0.2 and 0.4 °C (Figure 9b), while

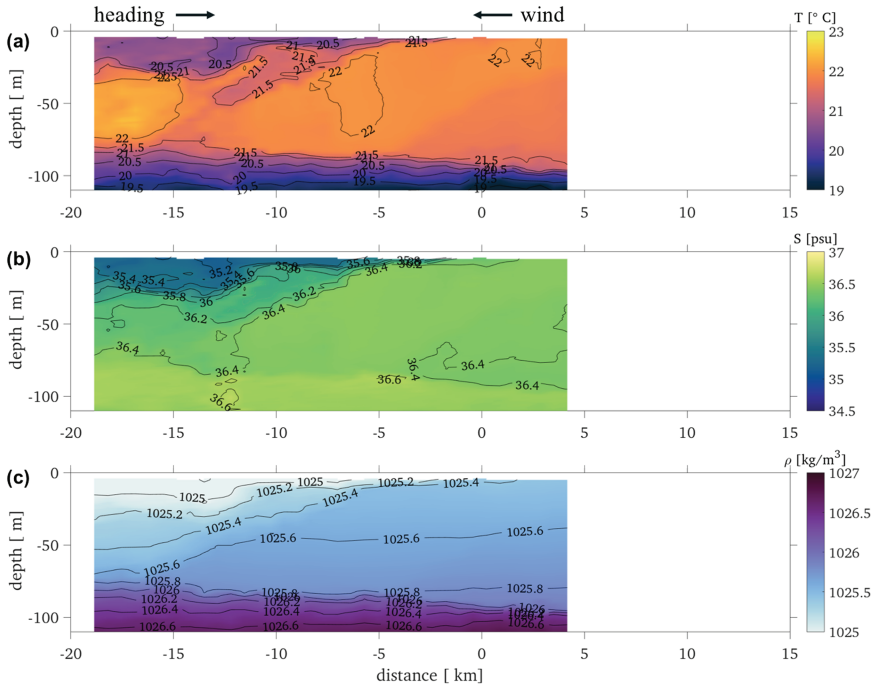

Figure 11. Vertical profiles along FT19. Wind is coming from right to left, and the R/V *Walton Smith* is translating from left to right. Front position denoted by "0." Temperature (a), salinity (b), and density (c) profiles derived from the moving vessel profiler are contoured.

ζ gradually increased from slightly unstable (−0.2) to near-neutral (0.05) conditions (Figure 9e). Also, sea level pressure increased about 0.2 hPa from the warm side to the cold side along each transect (Figure 9d).

For all transects, the wind speed generally decreased along the transect (Figure 9c). The largest decrease was observed for FT16, where there was a change of −1.5 m/s across the 5-km frontal crossing (Figure 9c). For all transects, except FT16, there was a distinct minimum in the momentum flux along the crossing, which for FT13 and FT17 occurred within 2 km of the frontal boundary (Figure 9f). For FT15 this occurred at ∼4 km downwind of the front. For FT16, the momentum flux monotonically decreased along the entire transect. For WC1, SHF, and LHF uniformly decreased along the transect, with changes about −20 and −50 W/m^2 for SHF and LHF (Figures 9g and 9h), respectively. These decreases were observed within 5 km downwind of the front.

4.1.4. Warm to Cold in Low Wind Condition

FT19 and FT21 were categorized as WC2 (Figure 10), due to their relatively low wind speed (U < 5 m/s). FT20 was excluded from the analysis due to a sudden change in wind direction (see Table 1 and Figure 2c) that may invalidate the analysis conducted here. The vertical profiles of water temperature and salinity along FT19 transect were shown in Figure 11, in which the colder (fresher) water occupied the upper ∼ 30 m on the downwind side. It displayed a trend of subduction (−14 to −10 km in Figure 11a) but did not form the analogous structure in Figure 4. The SST was still monotonically decreased. The vertical profile was consistent in WC2 group.

For WC2, SST decreased by 1.5 °C (Figure 12a), and the air temperature simultaneously decreased by ∼ 0.8 °C (Figure 12b). For FT19, ζ was near-neutral at and upwind of the front, but transitioned to fairly stable conditions over the downwind side out to −15 km (Figure 12e). For FT21, there was a slight transition from unstable to stable conditions between the warm and cold regions, with a distinct minimum centered around 3 km upwind of the front (Figure 12e). Along FT21, sea level pressure decreased by 0.8 hPa from WC, and FT19 exhibited a slight decreasing transition (0.3 hPa) across the front (Figure 12d).

In contrast to WC1, wind speeds were generally less than 5 m/s for FT19 and FT21 (Figure 12c). From the front to 15 km downwind, the wind speed along FT19 decreased by ∼2 m/s, while over a few kilometers across the front FT21, exhibited a mean wind decrease of < 1 m/s (Figure 12c). Away from the front, the

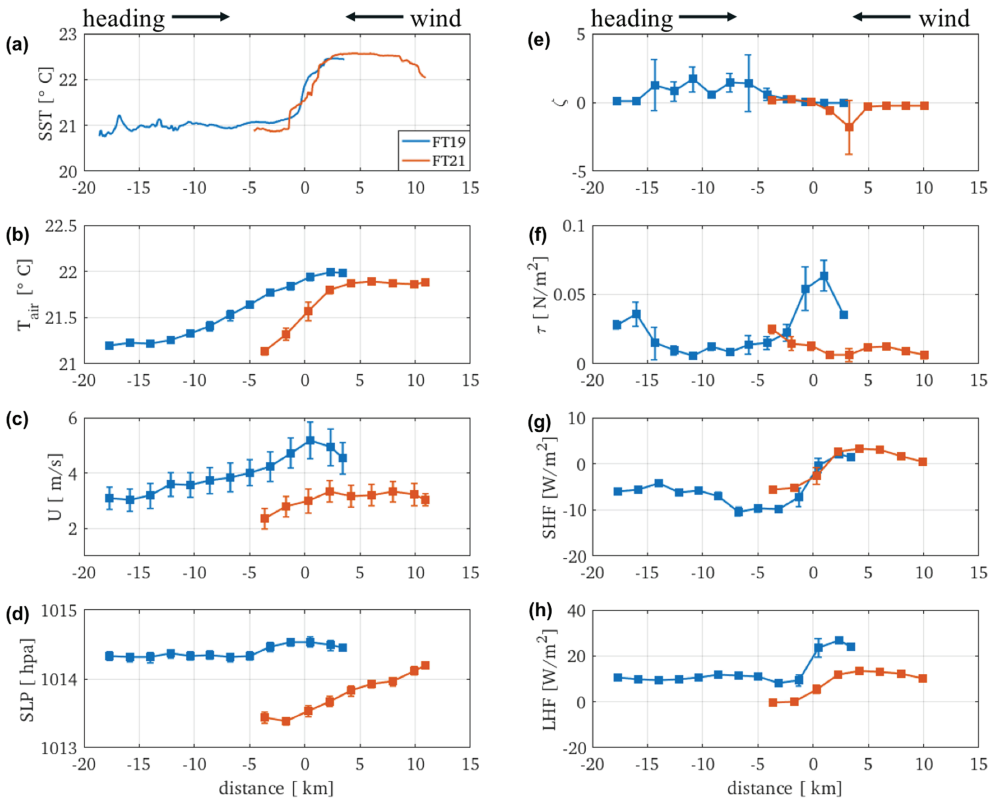

Figure 12. Observations from the starboard tower during the WC2 cross-frontal transects. (a) Sea surface temperature from flow-through MicroTSG, (b) air temperature, (c) 10-min averaged wind speed ($z = 5.3$ m), (d) sea level pressure ($z = 5.3$ m), (e) Monin-Obukhov stability parameter (ζ), (f) momentum flux, (g) sensible heat flux, and (h) latent heat flux derived using eddy covariance. The error bars indicate one standard deviation over each 10-min segment.

momentum flux was very low for both transects, which for FT21 was attributed to the low wind condition (Figure 12f). For FT19, a distinct peak in the momentum flux was observed around the front region, which collapsed to very low values (<0.01 N/m^2) within 3–5 km downwind of the front (Figure 12f). This transition in momentum flux was much faster (per unit kilometer) than the gradual change in wind speed observed for FT19. FT21 exhibited a trend of increasing momentum flux across the frontal boundary (Figure 12f), which actually countered the transition in wind speed (Figure 12c). The cross-front variation in SHF and LHF was similar between WC2 and WC1 (Figures 12g and 12h). Far away from the front, FT19 and FT21 both exhibited approximately the same SHF, with distinct changes in the flux coinciding with the SST gradient. For FT19, SHF showed a mean increase between −10 and −20 km from the front (Figure 12g). LHF was essentially constant for both transects on the cold side (Figure 12h, < -2 km).

4.2. ASL-SF Interaction After Accounting for Local Time Variability

The results presented above demonstrate that there is an observable response in the surface winds and air-sea fluxes to the presence of SFs. However, as it took around 1–2 hr to complete one cross-frontal transect, the direct impact of the frontal boundary on the surface wind speed may be obscured by the temporal variation of the large-scale motion. To isolate the SF effect on the ASL, the surface wind speed was compared with observations from a nearby NDBC platform—used because this is a stationary platform. In order to remove the temporal variation of the large-scale motion from the Walton Smith-observed time series, a linear regression was performed on the NDBC measurements over the same time period of each transect. Using the regression parameters, temporal trends derived from NDBC were isolated from the ship observed wind data (Figures 13a–13c); thus, the residual between the ship observation and the NDBC-derived regression represents the local surface wind variance. After performing this analysis for transects FT01 and FT03 in the CW condition, it was observed that a 1.5 °C increase of SST (within 6 km) led directly to a surface wind speed increase of nearly 2 m/s (Figure 13d). In the WC condition, the surface wind speed decreased

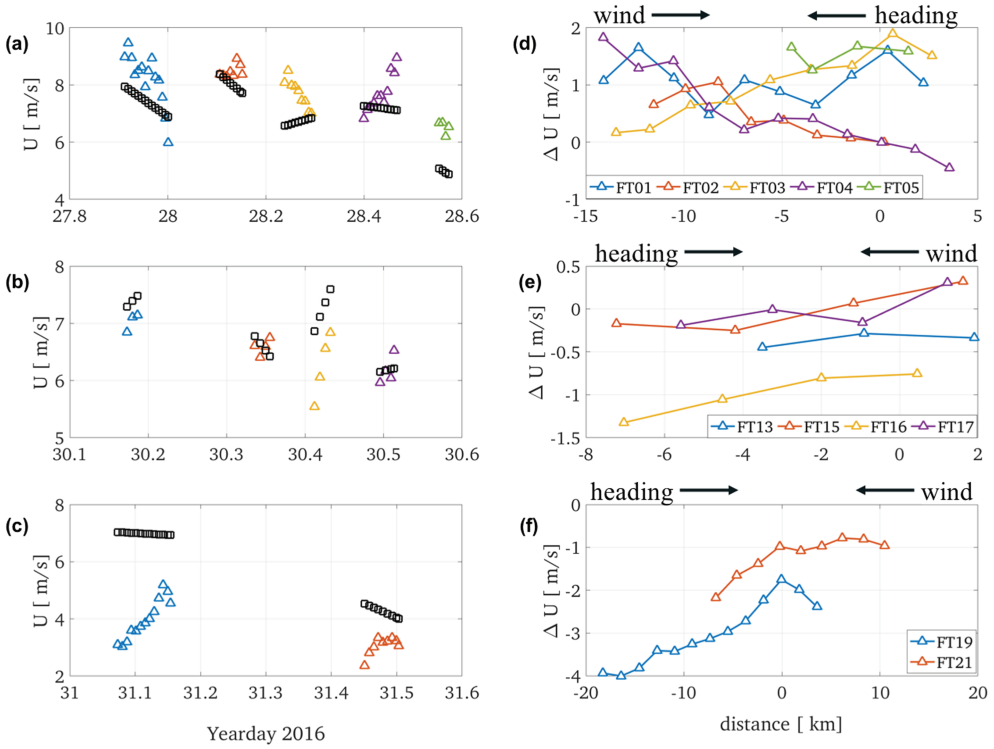

Figure 13. Wind speed from the shipboard observation and NDBC-derived fitted values. Observed wind speed (colored triangle) and linear fit value (black square) for each crossing wind speed in CW group (a), WC1 group (b) and WC2 group (c). The residual wind speed (observation minus linear fit wind speed) in CW group (d), WC1 group (e) and WC2 group (f). NDBC = National Data Buoy Center.

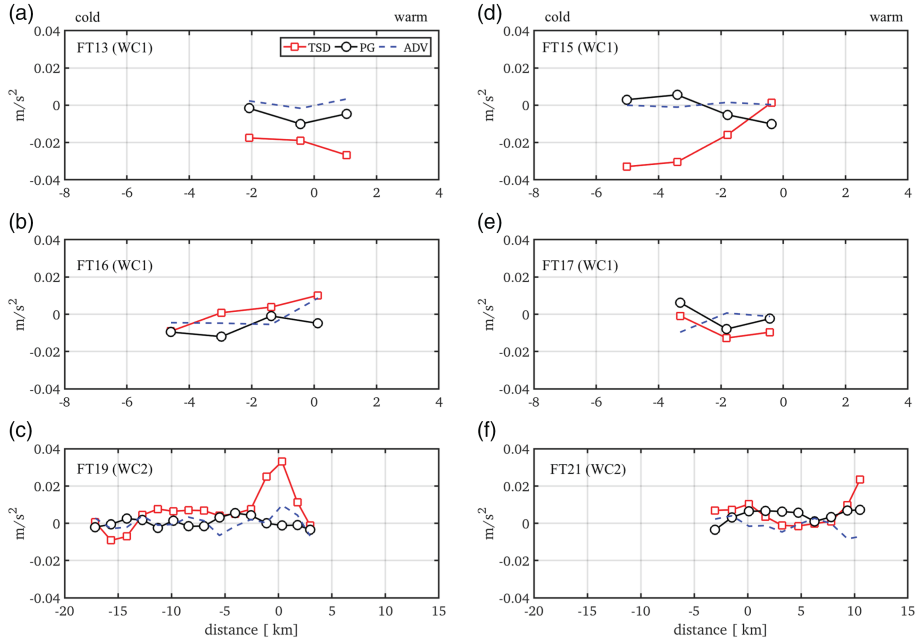

Figure 14. The resolved terms (TSD, PG, ADV) in the momentum budget from equation (15) for WC1 (FT13, FT15, FT16, FT17) and WC2 (FT19 and FT21). In these panels, the wind is coming from right to left. (a) FT13, (b) FT16, (c) FT19, (d) FT15, (e) FT17, and (f) FT21. TSD = turbulent stress divergence; PG = pressure gradient; ADV = advection.

(a)

	MF	SHF	LHF
N	1147	1105	1026
	85	81	80
S	0.73	0.66	0.83
	0.81	0.61	0.72
I	0.02	1.71	15.3
	0.01	-1.07	6.49
$\sqrt{MSE}$	0.04	10.8	34.8
	0.02	4.57	18.7
γ^2	0.73	0.91	0.9
	0.86	0.98	0.98

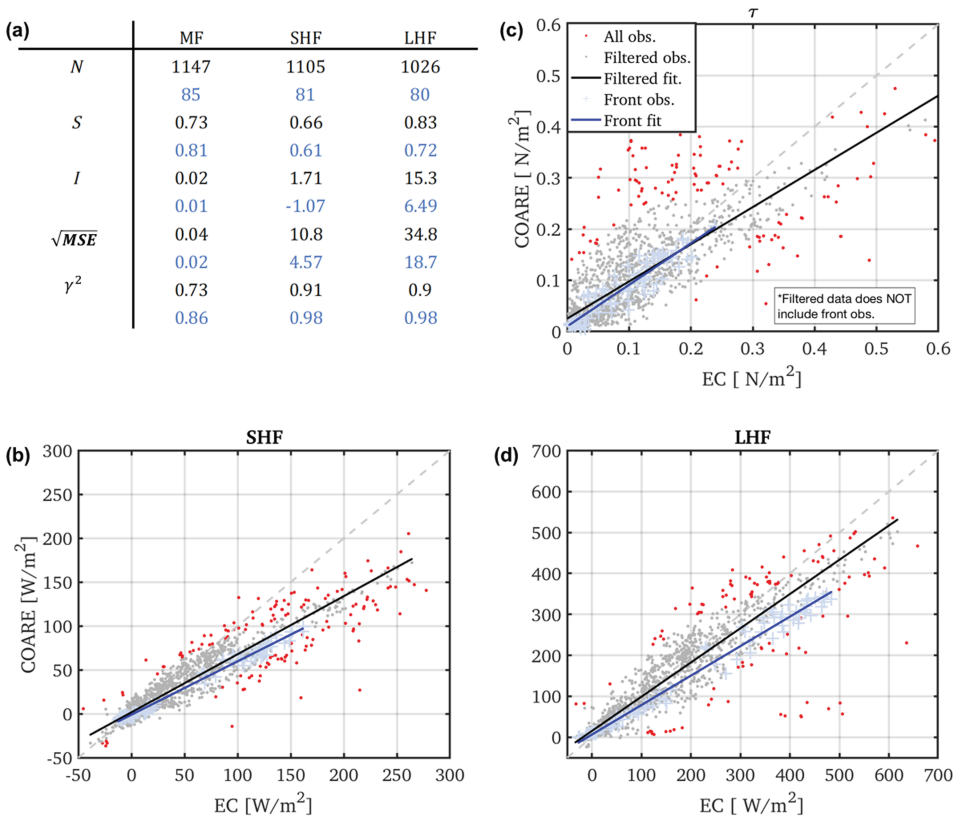

Figure 15. (a) Regression results for EC versus COARE 3.5 results: "N" is the number of data points; "S" is the slopes of each linear regressions; "I" is the corresponding intercept; "MSE" is the mean square error; "r^2" is the correlation coefficient of the linear model. The blue "+" denote the data points associated with frontal crossings. Regressions were perfomed on SHF (b), momentum flux (c), and LHF (d). EC = eddy covariance; SHF = sensible heat flux; LHF = latent heat flux.

about 0.5–1 m/s within 6 km (Figure 13e). The decrease was as large as 2 m/s over 15 km (FT19, Figure 13f) when the wind speed was lower than 5 m/s.

4.3. Momentum Budget Analysis

The momentum budget analysis was completed for WC1 and WC2, and here the focus will be on the explicitly resolved terms: ADV, PG, and TSD, while the residual will include contributions from the time-varying term. In WC condition, the ASL was generally close to neutral condition. CW transitions were not included in this analysis due to the strong convective conditions during those transects making it challenging to discern a clear ASL-SF interaction associated with the physical location of the frontal boundary.

In general, for WC1 (moderate winds), TSD was the dominant term in the budget. The mean value of TSD ranged from −0.04 to 0.01 m/s^2 (Figures 14a, 14b, 14d, and 14e). From the warm to the cold side, the TSD decreased by approximately 0.03, 0.02, and 0.005 m/s^2 along FT15, FT16, and FT17, respectively (Figures 14d, 14b, and 14e). However, the magnitudes of the TSD and PG did not show a clear pattern. The mean value of PG was generally negative, ranging from −0.01 to ~ 0 m/s^2 (Figures 14a, 14b, 14d, and 14e). It also corresponded the sea level pressure in Figure 9d. Additionally, the magnitude of ADV, close to 0, was the minimum term in this group. PG and TSD account for more than 90% of the total momentum across each of the transects in WC1.

In the WC2 (low winds) group, the relative significance of all the terms was similar to the WC1 results. The magnitude of TSD was generally between 0.01 to 0.04 m/s^2 (Figures 14c and 14f), which was 0.02 m/s^2 smaller than the average TSD for WC1. For FT19, TSD was observed to have a relatively large maximum above the SF (Figure 14c); while possibly expected, this distinct, localized peak in TSD could not be theoretically explained. Additionally, the magnitude of PG was close to 0 along FT19 transect (Figure 14c).

For FT21, TSD was near 0 to slightly positive over the warm side FT21 (Figure 14f) and PG was positive across most of FT21. The magnitude of ADV was close to 0 in these low wind conditions (Figures 14c and 14f).

4.4. Overall Flux Comparison

The EC fluxes (momentum flux, SHF, and LHF) were compared to COARE 3.5, both for the aggregate data sets and for the near-SFs observations, using linear, least squares regression (Figure 15). The results of the various regressions are provided in the table within Figure 15. A robust, iterative regression technique was used to determine the intercept and of the best fit slope between the bulk and direct flux values. Individual samples were rejected if their Cook's distance (Chatterjee & Hadi, 1986) exceeded a cutoff value of 1. This process removes overly influential samples from the total regression data set. This filtering was done independently for the aggregate and near-front data subsets. Furthermore, the regression on the aggregate data was done *without* including the near-front observations, in order to isolate the impact of the identified fronts from the general observations.

For momentum flux, an overall slope was observed between the EC and COARE 3.5 (Figure 15c), which did not significantly change weather or not one considered the near-front data or the aggregate, respectively. In general the momentum flux comparison was noisier than for SHF and LHF and larger stress values were not resolved in the present data set. For the SHF and LHF (Figures 15b and 15d), it was observed that the slopes between COARE 3.5 and EC decreased when only considering near-SF observations, as compared to the aggregate data. Ultimately, COARE 3.5 tended to underestimate the flux by 30–40%, implying the presence of SFs exacerbates the differences between EC and COARE estimated heat fluxes. It is important to note that the correlation between the EC and COARE 3.5 were fairly strong for both SHF and LHE ($r^2 > 0.9$), indicating that these observed slopes may be due to a systematic underestimation in the heat flux calculations (for COARE), rather than missing some key physical processes.

5. Discussion

5.1. Interpretation of ASL Response to SF

The magnitude of the localized surface wind speed gradient across the SFs was larger than what is associated with crossing warm/cold mesoscale eddy boundaries (see section 4.2). For instance, Frenger et al. (2013) observed eddies in the Southern Ocean where an anomaly of 0.5 °C SST caused 0.31 m/s variation of wind speed over ~100 km. Also, in the Kuroshio extension region, a 0.6 °C SST anomaly led to a 0.25 m/s change in surface wind speed (Ma et al., 2015). Wenegrat and Arthur (2018) showed that the changes in along-front velocity coupling coefficients near an SST-associated SF were an order of magnitude larger than previously observed mesoscale SST-wind, implying that the SF's impact on surface wind variation can be stronger than the impact of mesoscale fronts.

Interestingly, a noticeable 2–3 m/s deceleration of the surface wind speed within 20 km of the SF was observed in the CW condition (FT02 and FT04, Figure 13d). These findings contradict observations made across mesoscale front features (Friehe et al., 1991; Mahrt et al., 2004; Vickers & Mahrt, 2006) and numerical simulations of these processes (Kilpatrick et al., 2014; Skyllingstad et al., 2007). Combined with other features, such as the decreased air temperature (Figure 5b), nearly constant heat flux (Figures 5g and 5h), and decreasing wind speed (Figure 5c) along FT02 and FT04 transect, it is implied that there may exist secondary circulation or other complex structures near the front, as a case of pure ASL-front interaction could not explain these observed phenomena. The anomalous SST (Figure 5a) caused by the SF may contribute to the local circulation. Some previous observations (Friehe et al., 1991; Kwon et al., 1998) showed that secondary circulations occurred near SST fronts as well. Additionally, Gemmrich and Monahan (2018) posit that the variability in wind speed generates SST anomalies due to the enhanced air-sea heat fluxes and entrainment of colder water at the thermocline. Thus, they showed that there was a negative relationship between cross-frontal SST variation and wind speed variation in both the Pacific and Southern Oceans. These findings may apply at the submesoscale, though the observations in those previous works focused on the mesoscale dynamics.

Apart from the variation of surface wind speed, the momentum flux variation also showed interesting responses across SF. The minimum of momentum flux (Figure 9f) and the decreasing of wind speed (Figure 9c) may denote the location of an internal boundary layer (IBL), which may develop with the horizontal advection of an air mass across any discontinuity in the surface condition (Garratt, 1990). As expected

within the IBL, the strong gradient will increase the momentum flux and suppress the heat flux. Wind speed is retarded (Figure 9c) within the IBL owing to the increased stress divergence and accelerated above it (Garratt, 1990; Friehe et al., 1991). These observations may represent one of the first documented cases of an IBL forming over a SF. In the marine environment, IBLs are common in coastal areas (Mahrt, 2000; Klipp & Mahrt, 2003) and very recently have been associated with nonlinear internal ocean waves (Ortiz-Suslow et al., 2019). From our observations, IBLs were well developed during the WC condition (Figures 9 and 12), but it was not clearly shown in the unstable CW condition due to the enhanced convection upwind of the front (Figure 5c).

The sea level pressure variation across SFs was noticeable (Figures 5d, 9d, and 12d), though the scale of SF is one order smaller than mesoscale fronts and there the impact of SF on the pressure may not be strong. In CW and WC1 groups, the variation of sea level pressure (Figures 5d and 9d) was consistent with previous findings, namely, that higher pressure usually exists in the cold side of fronts (Friehe et al., 1991; Mahrt et al., 2004). However, higher pressure existed over the warm side of the front in WC2 (Figure 12d), which was different with the pattern observed at the mesoscale. An analogous phenomenon has been observed previously over the Brazilian shelf region (Pezzi et al., 2016). Our results may be attributed to a larger scale phenomena exerting an external force on the local ASL, which may explain our general findings in WC2 group as well.

In general, the variability and characteristics of ASL-SF interaction reported in this study hold implications for the numerical study of SFs. As the wind stress and surface cooling (heating) could largely affect the upper ocean potential vorticity (Thomas et al., 2013), adding the the role of SF on this variability could improve the fidelity of high resolution models. For example, these observations could inform on how to properly account for the relevant boundary conditions, on which previous studies do not reflect a standardized approach (Skyllingstad & Samelson, 2012). However, one of the significant limitations of this study was that the observations were confined to within 6 m above the sea surface. While this is critical to resolving the dynamics near the interface, the ability to draw more general conclusions about the depth into the ASL to which these effects are relevant is limited. How high this influence could reach is an open question and needs more observations.

5.2. Interpretation of the Momentum Budget Analysis

The directly estimated terms in the momentum budget were qualitatively consistent with previous LES simulation results (Skyllingstad et al., 2007) and observation (Friehe et al., 1991; Mahrt et al., 2004). The TSD was the dominant term in the momentum budget, which indicated that the momentum mixing contributed more than the PG in adjusting the wind profile, which was consistent with Vickers and Mahrt (2006) and Skyllingstad et al. (2007). These findings imply that some atmospheric eddies and/or coherent structures exist near the SF, which is causing the vertical momentum mixing to entrain larger momentum flux or high winds from above the ASL to near the interface (Small et al., 2008). This hypothesis was checked by using wavelet analysis of the high frequency (i.e., nonaveraged) winds and covariances. The results of this analysis showed that some coherent structures were present across SF, particularly over the warm side of the SF. This work is part of ongoing and future efforts and goes beyond the scope of this study.

The magnitude of these observed momentum budget terms is different from previous simulations studying the cross-frontal dynamics (Kilpatrick et al., 2014; Skyllingstad et al., 2007). In general, the estimated values of TSD and PG are between 10^{-3} and 10^{-2} m/s^2 (Figure 14), which is an order of magnitude larger than the numerical simulation results (Skyllingstad et al., 2007, 2014). Mahrt et al. (2018) emphasized that significant TSD may exist in the lowest 10 m of ASL that estimating the surface stress using observations at heights above the surface to extrapolate down to the interface is flawed. The effect of stability on the surface stress appears to be generally smaller than errors due to the stress divergence. The larger magnitude of TSD may be due to an IBL having formed over this relatively short horizontal distances (i.e., sharp gradients). In addition, the TSD vertical term ($\frac{\partial \overline{u'w'}}{\partial z}$) may be overestimated due to the short vertical interval (0.76 m). The relatively smaller value of the simulations (Skyllingstad et al., 2007; Kilpatrick et al., 2014) may also be caused by the models under-resolving the stress gradient. For example, Skyllingstad et al. (2007) used large eddy simulation model with a resolution of 4 m in vertical direction. This grid resolution may be too coarse to capture the TSD variability above the SFs. As direct measurements of TSD are rare over the ocean, the discrepancy between this observation and related simulation results is expected. Further investigation is warranted to further elucidate the divergence between observations and models in this regime.

5.3. Enhanced Air-Sea Heat Flux

The comparison between EC and COARE 3.5 (Figure 15) showed an enhancement of heat flux associated with the presence of SFs, which could be attributed to several individual factors. For example, the convergence at a SF can result in the water mass subducting at rates of 10–100 m/day, compared to typical rates of 1–10 m/day (an order of magnitude less) over an ambient ocean surface (Ferrari, 2011). The rapid vertical velocities may also lead to the enhancement of sub-surface turbulence, which may contribute to the enhancement of air-sea heat flux (D'Asaro, 2014; Esters et al., 2018). The enhancement may also affect the exchange rate of heat and other gases between the atmosphere and the ocean (Esters et al., 2017). A recent simulation (Su et al., 2018) showed that upper-ocean, submesoscale turbulence produced a systematical upward vertical heat transport, with winter time averages up to 100 W/m^2 for mid-latitudes. In addition, the wave-current interaction near SFs would enhance the wave breaking near SFs (Romero et al., 2017) and breaking waves are known to increase momentum flux and heat flux (Banner & Melville, 1976), which may also account for the enhancement of heat flux.

As the air-sea heat flux was larger than COARE 3.5, the heat flux parameterization over a heterogeneous SST surface may need to be modified as compared to homogeneous conditions. For example, SHF was positive in the warm side but negative in the cold side (Figure 9g), which was consistent with the transition in air-sea temperature difference. This kind of SST heterogeneity could contribute significantly to the counter-gradient flux (Mahrt & Hristov, 2017; Mahrt & Khelif, 2010; Vickers & Mahrt, 2006; Vihma et al., 1998). In a sharp SST gradient front (e.g., 7 °C within 10 km in Mahrt et al., 2004), the bulk gradient (air-sea temperature difference) averaged over the track may be negative, yet the averaged heat flux could be positive. This was also noted in Vickers and Mahrt (2006).

6. Conclusion

The goal of this study was to investigate the impact of SF on surface winds and air-sea fluxes using direct near surface measurements of air-sea interaction variables collected during a large number of cross-frontal transects. The results of this work showed that the surface wind in CW condition did not show a uniform behavior under the strongly unstable regime. Both acceleration and deceleration of surface wind across SFs were observed, and they were temporally mixed. The acceleration was consistent with previous observations, but the deceleration of surface wind may be induced by secondary circulations near the SF. In the WC condition, the surface wind speed decreased consistently and the air-sea temperature difference indicated these WC observations were made within a near-neutral regime.

In addition, analysis of the cross-frontal momentum budget for the WC group generally supported that concept of TSD being the dominant term, accounting for 20–80%, while the pressure gradient generally accounted for < 20% of the total budget. The mechanism of surface wind deceleration across SFs was analogous with previous studies focused on the mesoscale regime (Friehe et al., 1991; Kilpatrick et al., 2014). This implies that the mechanisms used to describe mesoscale frontal, air-sea interaction may apply to the submesoscale regime.

Aside from the surface wind variation, the SF made a clear thermal imprint on the ASL. The air temperature and heat flux consistently varied with the local SST across the fronts. The directly observed heat fluxes were generally 1.5 times larger than COARE 3.5 output, for the same equivalent mean wind speed, temperature, and humidity, when a SF was present. This suggests that SF drive localized enhancement of the heat flux that is not fully resolved by the bulk formulae. As SFs over the global ocean are common, the enhancement bears significance for the global energy balance. The findings of this study provide some caution to relying on the bulk estimates of the fluxes in locales where there is strong surface heterogeneity, such as in the vicinity of SF or other similar scale gradients and discontinuities (e.g., eddies and filaments).

Acknowledgments

The work was supported by Gulf of Mexico Research Initiative (Grant SA-1515 CARTHE). LASER data are publicly available through the Gulf of Mexico Research Initiative Information & Data Cooperative (GRIIDC) at https://data.gulfresearchinitiative.org under the following DOIs: 10.7266/N7S75DRP (shipboard meteorological data), 10.7266/n7-93j3-mn56 (shipboard ADCP), 10.7266/N7N01550 (radar), 10.7266/N7H130FC (MVP), and 10.7266/N7W0940J (drifters). NDBC buoy data is available at https://www.ndbc.noaa.gov/station_page.php?station=42887. The authors greatly appreciate the tremendous efforts of the *Walton Smith* Captain and Crew, as well as other members of the LASER field study team. We would especially like to thank the efforts of Mike Rebozo in the design and execution of the field work. The insight and input of Darek Bogucki and William M. Drennan were very helpful during the data processing and analysis phases of this work. We thank the Editor and three anonymous reviewers for their constructive suggestions.

References

Anctil, F., Donelan, M. A., Drennan, W. M., & Graber, H. C. (1994). Eddy-correlation measurements of air-sea fluxes from a discus buoy. *Journal of Atmospheric and Oceanic technology*, *11*(4), 1144–1150.

Banner, M., & Melville, W. (1976). On the separation of air flow over water waves. *Journal of fluid mechanics*, *77*(4), 825–842.

Businger, J. A., et al. (1971). Flux-profile relationships in the atmospheric surface layer. *Journal of the atmospheric Sciences*, *28*(2), 181–189.

Byrne, D., Münnich, M., Frenger, I., & Gruber, N. (2016). Mesoscale atmosphere ocean coupling enhances the transfer of wind energy into the ocean. *Nature communications*, *7*, ncomms11867.

Capet, X., McWilliams, J. C., Molemaker, MJeroen, & Shchepetkin, A. (2008). Mesoscale to submesoscale transition in the California Current System. part ii: Frontal processes. *Journal of Physical Oceanography*, *38*(1), 44–64.
Chatterjee, S., & Hadi, A. S. (1986). Influential observations, high leverage points, and outliers in linear regression. *Statistical Science*, *1*(3), 379–393.
Chelton, D. B., Schlax, M. G., Freilich, M. H., & Milliff, R. F. (2004). Satellite measurements reveal persistent small-scale features in ocean winds. *Science*, *303*(5660), 978–983.
Chelton, D. B., & Xie, S.-P. (2010). Coupled ocean-atmosphere interaction at oceanic mesoscales. *Oceanography*, *23*(4), 52–69.
D'Asaro, E. A. (2014). Turbulence in the upper-ocean mixed layer. *Annual Review of Marine Science*, *6*, 101–115.
D'Asaro, E. A., Lee, C., Rainville, L., Harcourt, R. R., & Thomas, L. (2011). Enhanced turbulence and energy dissipation at ocean fronts. *Science*, *3326027*, 318–22.
D'Asaro, E. A., Shcherbina, A. Y., Klymak, J. M., Molemaker, J., Novelli, G., Guigand, C. M., et al. (2018). Ocean convergence and the dispersion of flotsam. *Proceedings of the National Academy of Sciences*, *115*(6), 1162–1167.
Edson, J. B., Jampana, V., Weller, R. A., Bigorre, S. P., Plueddemann, A. J., Fairall, C. W., et al. (2013). On the exchange of momentum over the open ocean. *Journal of Physical Oceanography*, *43*(8), 1589–1610.
Esters, L., Breivik, Ø., Landwehr, S., ten Doeschate, A., Sutherland, G., Christensen, K. H., et al. (2018). Turbulence scaling comparisons in the ocean surface boundary layer. *Journal of Geophysical Research: Oceans*, *123*, 2172–2191. https://doi.org//10.1002/2017JC013525
Esters, L., Landwehr, S., Sutherland, G., Bell, T. G., Christensen, K. H., Saltzman, E. S., et al. (2017). Parameterizing air-sea gas transfer velocity with dissipation. *Journal of Geophysical Research: Oceans*, *122*, 3041–3056. https://doi.org/10.1002/2016JC012088
Fairall, C. W., Bradley, E. F., Hare, J., Grachev, A., & Edson, J. (2003). Bulk parameterization of air–sea fluxes: Updates and verification for the COARE algorithm. *Journal of Climate*, *16*(4), 571–591.
Fairall, C. W., Bradley, E. F., Rogers, D. P., Edson, J. B., & Young, G. S. (1996). Bulk parameterization of air-sea fluxes for tropical ocean-global atmosphere coupled-ocean atmosphere response experiment. *Journal of Geophysical Research*, *101*(C2), 3747–3764.
Ferrari, R. (2011). A frontal challenge for climate models. *Science*, *332*(6027), 316–317.
Frenger, I., Gruber, N., Knutti, R., & Münnich, M. (2013). Imprint of southern ocean eddies on winds, clouds and rainfall. *Nature Geoscience*, *6*(8), 608.
Friehe, C., Shaw, W., Rogers, D., Davidson, K., Large, W., Stage, S., et al. (1991). Air-sea fluxes and surface layer turbulence around a sea surface temperature front. *Journal of Geophysical Research*, *96*(C5), 8593–8609.
Garratt, J. (1990). The internal boundary layer—A review. *Boundary-Layer Meteorology*, *50*(1-4), 171–203.
Gaube, P., Chickadel, C., Branch, R., & Jessup, A. (2019). Satellite observations of SST-induced wind speed perturbation at the oceanic submesoscale. *Geophysical Research Letters*, *46*, 2690–2695. https://doi.org/10.1029/2018GL080807
Geernaert, KristinaB, & Richter, K. (1986). Variation of the drag coefficient and its dependence on sea state. *Journal of Geophysical Research*, *91*(C6), 7667–7679.
Gemmrich, J., & Monahan, A. (2018). Covariability of near-surface wind speed statistics and mesoscale sea surface temperature fluctuations. *Journal of Physical Oceanography*, *48*(3), 465–478.
Goring, D. G., & Nikora, V. I. (2002). Despiking acoustic Doppler velocimeter data. *Journal of Hydraulic Engineering*, *128*(1), 117–126.
Högström, U., Rutgersson, A., Sahlée, E., Smedman, A.-S., Hristov, T. S., Drennan, W. M., & Kahma, K. (2013). Air–sea interaction features in the Baltic Sea and at a Pacific trade-wind site: An inter-comparison study. *Boundary-layer meteorology*, *147*(1), 139–163.
Högström, U., Sahlée, E., Drennan, W. M., Kahma, K. K., Smedman, A.-S., Johansson, C., et al. (2008). Momentum fluxes and wind gradients in the marine boundary layer-a multi-platform study. *Boreal Environment Research Publishing Board*, *13*, 475–502.
Katsaros, K. B., Donelan, M. A., & Drennan, W. M. (1993). Flux measurements from a SWATH ship in SWADE. *Journal of Marine Systems*, *4*(2-3), 117–132.
Kilpatrick, T., Schneider, N., & Qiu, B. (2014). Boundary layer convergence induced by strong winds across a midlatitude SST front. *Journal of Climate*, *27*(4), 1698–1718.
Klein, P., Lapeyre, G., Siegelman, L., Qiu, B., Fu, L.-L., Torres, H., et al. (2019). Ocean-scale interactions from space. *Earth and Space Science*, *6*(5), 795–817.
Klipp, C., & Mahrt, L. (2003). Conditional analysis of an internal boundary layer. *Boundary-layer meteorology*, *108*(1), 1–17.
Kwon, B., Bénech, B, Lambert, D., Durand, P., Druilhet, A., Giordani, H., & Planton, S. (1998). Structure of the marine atmospheric boundary layer over an oceanic thermal front: Semaphore experiment. *Journal of Geophysical Research*, *103*(C11), 25,159–25,180.
Lambaerts, J., Lapeyre, G., Plougonven, R., & Klein, P. (2013). Atmospheric response to sea surface temperature mesoscale structures. *Journal of Geophysical Research: Atmospheres*, *118*, 9611–9621. https://doi.org/10.1002/jgrd.50769
Lindzen, R. S., & Nigam, S. (1987). On the role of sea surface temperature gradients in forcing low-level winds and convergence in the tropics. *Journal of the Atmospheric Sciences*, *44*(17), 2418–2436.
Lohmann, R., & Belkin, I. M. (2014). Organic pollutants and ocean fronts across the atlantic ocean: A review. *Progress in Oceanography*, *128*, 172–184.
Lund, B., Graber, H. C., Tamura, H., Collins, C., & Varlamov, S. (2015). A new technique for the retrieval of near-surface vertical current shear from marine X-band radar images. *Journal of Geophysical Research: Oceans*, *120*, 8466–8486. https://doi.org/10.1002/2015JC010961
Lund, B., Haus, B. K., Horstmann, J., Graber, H. C., Carrasco, R., Laxague, N. J., et al. (2018). Near-surface current mapping by shipboard marine X-band radar: A validation. *Journal of Atmospheric and Oceanic Technology*, *35*(5), 1077–1090.
Ma, Jing, Z., Chang, P., Liu, X., Montuoro, R., Small, R. J., et al. (2016). Western boundary currents regulated by interaction between ocean eddies and the atmosphere. *Nature*, *535*(7613), 533.
Ma, Xu, H., Dong, C., Lin, P., & Liu, Y. (2015). Atmospheric responses to oceanic eddies in the Kuroshio extension region. *Journal of Geophysical Research: Atmospheres*, *120*, 6313–6330. https://doi.org/10.1002/2014JD022930
MacKinnon, J. A., Zhao, Z., Whalen, C. B., Waterhouse, A. F., Trossman, D. S., Sun, O. M., et al. (2017). Climate process team on internal wave–driven ocean mixing. *Bulletin of the American Meteorological Society*, *98*(11), 2429–2454.
Mahrt, L. (2000). Surface heterogeneity and vertical structure of the boundary layer. *Boundary-Layer Meteorology*, *96*(1-2), 33–62.
Mahrt, L., & Hristov, T. (2017). Is the influence of stability on the sea surface heat flux important? *Journal of Physical Oceanography*, *47*(3), 689–699.
Mahrt, L., & Khelif, D. (2010). Heat fluxes over weak SST heterogeneity. *Journal of Geophysical Research*, *115*, D11103. https://doi.org/10.1029/2009JD013161
Mahrt, L., Miller, S., Hristov, T., & Edson, J. (2018). On estimating the surface wind stress over the sea. *Journal of Physical Oceanography*, *48*(7), 1533–1541.
Mahrt, L., Vickers, D., & Moore, E. (2004). Flow adjustments across sea-surface temperature changes. *Boundary-layer Meteorology*, *111*(3), 553–564.

McWilliams, J. C. (2016). Submesoscale currents in the ocean. *Proceedings of the Royal Society A: Mathematical, Physical and Engineering Sciences*, *472*(2189), 20160117.
Minobe, S., Kuwano-Yoshida, A., Komori, N., Xie, S.-P., & Small, R. J. (2008). Influence of the Gulf Stream on the troposphere. *Nature*, *452*(7184), 206.
Monin, A. S., & Obukhov, A. M. (1954). Basic laws of turbulent mixing in the surface layer of the atmosphere. *Proceedings of Geophysics Institute, National Academy of Science, SSSR*, *151*(163), e187.
Nonaka, M., & Xie, S.-P. (2003). Covariations of sea surface temperature and wind over the Kuroshio and its extension: Evidence for ocean-to-atmosphere feedback. *Journal of climate*, *16*(9), 1404–1413.
O'Neill, L. W. (2012). Wind speed and stability effects on coupling between surface wind stress and SST observed from buoys and satellite. *Journal of Climate*, *25*(5), 1544–1569.
O'Neill, L. W., Chelton, D. B., & Esbensen, S. K. (2012). Covariability of surface wind and stress responses to sea surface temperature fronts. *Journal of Climate*, *25*(17), 5916–5942.
O'Neill, L. W., Haack, T., Chelton, D. B., & Skyllingstad, E. (2017). The Gulf Stream convergence zone in the time-mean winds. *Journal of the Atmospheric Sciences*, *74*(7), 2383–2412.
Ortiz-Suslow, D., Haus, B., Williams, N., Graber, H. C., & MacMahan, J. H. (2018). Observations of air-sea momentum flux variability across the inner shelf. *Journal of Geophysical Research: Oceans*, *123*, 8970–8993. https://doi.org/10.1029/2018JC014348
Ortiz-Suslow, D., Haus, B. K., Williams, N., Laxague, N., Reniers, A., & Graber, H. C. (2015). The spatial-temporal variability of air-sea momentum fluxes observed at a tidal inlet. *Journal of Geophysical Research: Oceans*, *120*, 660–676. https://doi.org/10.1002/2014JC010412
Ortiz-Suslow, D., Wang, Q., Kalogiros, J., Yamaguchi, R., De Paolo, T., Terrill, E., et al. (2019). Interactions between nonlinear internal ocean waves and the atmosphere. *Geophysical Research Letters*, *46*, 9291–9299. https://doi.org/10.1029/2019GL083374
Pezzi, L., Souza, R., Farias, P., Acevedo, O., & Miller, A. (2016). Air-sea interaction at the southern Brazilian continental shelf: In situ observations. *Journal of Geophysical Research: Oceans*, *121*, 6671–6695. https://doi.org/10.1002/2016JC011774
Plagge, A., Edson, J. B., & Vandemark, D. (2016). In situ and satellite evaluation of air–sea flux variation near ocean temperature gradients. *Journal of Climate*, *29*(4), 1583–1602.
Poje, A. C., Özgökmen, T. M., Lipphardt, B. L., Haus, B. K., Ryan, E. H., Haza, A. C., et al. (2014). Submesoscale dispersion in the vicinity of the deepwater horizon spill. *Proceedings of the National Academy of Sciences*, *111*(35), 12,693–12,698.
Renault, L., Marchesiello, P., Masson, S., & McWilliams, J. C. (2019). Remarkable control of western boundary currents by eddy killing, a mechanical air-sea coupling process. *Geophysical Research Letters*, *46*, 2743–2751. https://doi.org/10.1029/2018GL081211
Romero, L., Lenain, L., & Melville, W. K. (2017). Observations of surface wave–current interaction. *Journal of Physical Oceanography*, *47*(3), 615–632.
Samelson, R., Skyllingstad, E., Chelton, D., Esbensen, S., O'Neill, L., & Thum, N. (2006). On the coupling of wind stress and sea surface temperature. *Journal of Climate*, *19*(8), 1557–1566.
Shi, R., Chen, J., Guo, X., Zeng, L., Li, J., Xie, Q., et al. (2017). Ship observations and numerical simulation of the marine atmospheric boundary layer over the spring oceanic front in the northwestern South China Sea. *Journal of Geophysical Research: Atmospheres*, *122*, 3733–3753. https://doi.org/10.1002/2016JD026071
Skyllingstad, E. D., & Samelson, R. (2012). Baroclinic frontal instabilities and turbulent mixing in the surface boundary layer. Part i: Unforced simulations. *Journal of Physical Oceanography*, *42*(10), 1701–1716.
Skyllingstad, E. D., Vickers, D., Mahrt, L., & Samelson, R. (2007). Effects of mesoscale sea-surface temperature fronts on the marine atmospheric boundary layer. *Boundary-Layer Meteorology*, *123*(2), 219–237.
Small, R. J. d, Xie, S., O'Neill, L, Seo, H., Song, Q., Cornillon, P., et al. (2008). Air–sea interaction over ocean fronts and eddies. *Dynamics of Atmospheres and Oceans*, *45*(3-4), 274–319.
Song, Q., Cornillon, P., & Hara, T. (2006). Surface wind response to oceanic fronts. *Journal of Geophysical Research*, *111*, C12006. https://doi.org/10.1029/2006JC003680
Su, Z., Wang, J., Klein, P., Thompson, A. F., & Menemenlis, D. (2018). Ocean submesoscales as a key component of the global heat budget. *Nature Communications*, *9*(1), 775.
Sullivan, P. P., & McWilliams, J. C. (2018). Frontogenesis and frontal arrest of a dense filament in the oceanic surface boundary layer. *Journal of Fluid Mechanics*, *837*, 341–380.
Taylor, J. R. (2018). Accumulation and subduction of buoyant material at submesoscale fronts. *Journal of Physical Oceanography*, *48*(6), 1233–1241.
Tennekes, H., Lumley, J. L., & Lumley, J. (1972). *A first course in turbulence*. Boston, MA: MIT Press.
Thomas, L. N., Tandon, A., & Mahadevan, A. (2008). Submesoscale processes and dynamics. *Ocean modeling in an Eddying Regime*, *177*, 17–38.
Thomas, L. N., Taylor, J. R., Ferrari, R., & Joyce, T. M. (2013). Symmetric instability in the Gulf Stream. *Deep Sea Research Part II: Topical Studies in Oceanography*, *91*, 96–110.
Veron, F., Melville, W. K., & Lenain, L. (2008). Wave-coherent air–sea heat flux. *Journal of Physical Oceanography*, *38*(4), 788–802.
Vickers, D., & Mahrt, L. (2006). Evaluation of the air-sea bulk formula and sea-surface temperature variability from observations. *Journal of Geophysical Research*, *111*, C05002. https://doi.org/10.1029/2005JC003323
Vihma, T., Uotila, J., & Launiainen, J. (1998). Air-sea interaction over a thermal marine front in the Denmark Strait. *Journal of Geophysical Research*, *103*(C12), 27,665–27,678.
Wallace, J. M., Mitchell, T. P., & Deser, C. (1989). The influence of sea-surface temperature on surface wind in the eastern equatorial Pacific: Seasonal and interannual variability. *Journal of Climate*, *2*(12), 1492–1499.
Wenegrat, J., & Arthur, R. (2018). Response of the atmospheric boundary layer to submesoscale sea surface temperature fronts. *Geophysical Research Letters*, *45*, 13,505–13,512. https://doi.org/10.1029/2018GL081034
Xu, M., & Xu, H. (2015). Atmospheric responses to Kuroshio SST front in the East China Sea under different prevailing winds in winter and spring. *Journal of Climate*, *28*(8), 3191–3211.